Vrije Universiteit Brussel

Faculteit Wetenschappen
Departement Natuurkunde

Search for stop quarks using the matrix element method at the LHC

Proefschrift ingediend met het oog op het behalen van de graad van Master in de Wetenschappen

Lieselotte Moreels

Promotor: Prof. Dr. Jorgen D'Hondt
Co-promotor: Dr. Petra Van Mulders

Academiejaar 2012–2013

Contents

1 Introduction **1**

2 Beyond the Standard Model **3**

2.1 The Standard Model 3
2.2 The Hierarchy Problem 5
2.3 Supersymmetry 7
  2.3.1 The Minimal Supersymmetric Standard Model 8
  2.3.2 The constrained MSSM 9
  2.3.3 Simplified models 9
    2.3.3.1 Direct stop quark pair production 10
    2.3.3.2 State of the art 11

3 Observation of New Particles **13**

3.1 The Large Hadron Collider 14
3.2 The Compact Muon Solenoid Experiment 16
  3.2.1 Coordinate system 16
  3.2.2 The inner tracker 17
  3.2.3 The calorimeter system 18
  3.2.4 The muon system 19
3.3 Trigger and Data Aquisition 20

4 Reconstruction of Particles **21**

4.1 Identification of Particles 21
4.2 Object Reconstruction in the Subdetectors 22
  4.2.1 Track reconstruction in the inner tracker 22
  4.2.2 Reconstruction of energy deposits in the calorimeters 24
  4.2.3 Track reconstruction in the muon system 24
4.3 The Particle Flow Algorithm 25
  4.3.1 Muon reconstruction 25
  4.3.2 Electron reconstruction 26
  4.3.3 Jet reconstruction 27
    4.3.3.1 Identification of b jets 28
    4.3.3.2 Removal of isolated leptons 29

5 Event Selection **31**
5.1 Event Topology . . . 31
5.2 Event Generation and Simulation . . . 32
5.3 Selection Requirements . . . 34

6 Event Reconstruction **39**
6.1 Jet-Parton Matching . . . 39
6.2 Jet-Parton Association . . . 40

7 The Matrix Element Method **43**
7.1 The Matrix Element Method in a Nutshell . . . 43
7.2 Implementation in MadWeight . . . 45

8 Sensitivity of the Matrix Element Method for Stop Quark Searches **49**
8.1 Calculation of the Probability Density for Different Hypotheses . . 49
8.2 Sensitivity of Different Observables . . . 50
8.2.1 Likelihood ratio . . . 50
8.2.2 Regular kinematic observable . . . 52
8.2.3 Transformation of the likelihood ratio . . . 53
8.3 Upper Limit on the Signal Cross Section . . . 55

9 Conclusions & Perspectives **59**

10 Summary **61**

Samenvatting **63**

Acknowledgements **65**

References **67**

List of Abbreviations **75**

Appendix A Jet Reconstruction Algorithms **77**
A.1 Iterative Cone Algorithms . . . 77
A.2 Sequential Recombination Algorithms . . . 78

Appendix B b-tag Scale Factors **81**

Appendix C MadWeight Cards **83**
C.1 Process Cards . . . 83
C.2 Transfer Function . . . 85
C.3 MadWeight Card . . . 86

1

Introduction

One of the greatest achievements of the twentieth century is the standard model of particle physics. Even so, it has been clear for a while now that theories beyond the standard model are required to describe all aspects of the observable universe. One such theory is supersymmetry, which gained popularity as it can provide an answer to many of the standard model's short-comings. This theory introduces many new particles and thus also new physics processes. Since they have not yet been discovered, it is expected that they have a very low production rate. Therefore, dedicated analysis techniques are developed to differentiate between a small signal and a huge background, originating from standard model processes.

The matrix element method was developed at the Tevatron collider in order to make a more precise measurement of the top quark mass. It uses the theoretical matrix element of a process to determine the probability that this process is observed for specific values of the theoretical parameters. So far, it has not yet been used at the LHC to search for new physics processes.

This thesis investigates if the matrix element method is a viable technique to do so. To this purpose, a simplified supersymmetric model is used as a case study. The simplified model considers direct stop quark pair production, where the stop quark decays into a top quark and a neutralino. The expected upper limit on the cross section of this process will be used as a measure of the performance of this technique. It will be determined in one point of the $(m_{\tilde{\mathrm{t}}}, m_{\tilde{\chi}^0})$ parameter space, namely where the stop quark mass is 350 GeV and the mass of the neutralino is 100 GeV. To lighten the notation, natural units ($c = 1 = \hbar$) are used.

If the result is to be compared with those of dedicated analysis techniques and published results, a full study of the systematic uncertainties has to be carried out. This is beyond the scope of this thesis. Instead, the expected upper limit that is determined by the matrix element method is compared to that obtained with a simple kinematic variable, $H_{\mathrm{T}} + \not{E}_{\mathrm{T}}$. If the matrix element method is more sensitive to the signal, it should produce a stronger exclusion limit than the kinematic variable.

Chapter 2 will briefly describe the theoretical foundations of this thesis. A short overview of the standard model particles and forces is given and, via the hierarchy problem, the basics of supersymmetry, especially the MSSM, are introduced.

Chapter 3 elaborates on how particles are observed. Apart from the collider set-up, it also discusses the CMS experiment, that observes the remnants of the collisions produced by the LHC.

Chapter 4 describes how the electronic detector signals that are produced by these remnants can be reconstructed into particles. To this purpose, the particle flow algorithm is used.

The signal topology is explained in Chapter 5. This analysis will only consider events with a semi-muonic decay. Also the main backgrounds are defined, as well as the selection requirements to select the events and to increase the signal-to-background ratio. The observed data are complemented by simulated signal and background samples to correctly estimate their respective effects.

The event topology is reconstructed in Chapter 6. The parton information of the $\mathrm{t\bar{t}}$ background sample is used to reconstruct the hadronically decaying W boson and its corresponding top quark. This allows for their masses to be estimated. A χ^2 method employing these masses is used to assign jets to partons.

Chapter 7 describes the basic components of the matrix element method and the program that is used to process it, while Chapter 8 contains the results of the probability calculations. A variable that discriminates between signal and background is constructed and its sensitivity compared to that of $H_\mathrm{T} + \not{E}_\mathrm{T}$.

2

Beyond the Standard Model

The observable world, its elementary particles and their interactions, can be described by the Standard Model of particle physics (SM). The final piece of the puzzle seems to be in place with the discovery of the Brout–Englert–Higgs boson—in the remaining text referred to as the Higgs boson. Yet, despite the model's excellent agreement with precision measurements, there are still some questions that the SM cannot answer. For example, the observed 'dark matter' does not behave like the 'ordinary matter' described by the SM, not to mention the enigmatic 'dark energy'. In addition, the enormous tuning necessary to solve the hierarchy problem can hardly be called natural. Physicists have to look at so-called BSM-theories (Beyond the Standard Model) to find a solution for these problems, though most theories can only solve some of the SM's weak spots.

A very promising BSM-theory is Supersymmetry (SUSY) [1]. Here, a new symmetry between fermions and bosons is introduced. This results in supersymmetric partners for all SM particles. Many supersymmetric models have been theoretically worked out in great detail, but none of them have yet been experimentally observed. If a Higgs boson with the observed mass of about 126 GeV is to be included in the model, the parameter space of SUSY is substantially reduced. Moreover, to get a natural solution for the hierarchy problem, mass restrictions can be imposed on the supersymmetric particles. For the top squark—or stop quark—, the supersymmetric partner of the top quark, this results in relatively low masses, of the order TeV or lower, which brings it within the range of the Large Hadron Collider.

2.1 The Standard Model

The SM describes the world of elementary particles and the forces acting on them. The matter particles are divided into two groups, quarks and leptons. The group of quarks consists of up-type quarks—the up, charm and top quark—and down-type quarks—the down, strange and bottom quark. The lepton group consists of neutrinos and electrons, muons and taus. These are arranged into three generations or families of particles, where each generation is heavier than the previous. This is visualised in Figure 2.1 [2]. The quarks and leptons that are placed on the same row have the same properties. The electron, and accordingly also the muon and tau, has an electric charge of $-e$, where $e = 1.602\,10^{-19}\,\mathrm{C}$ [3] is the elementary charge. Up-type quarks have a charge of $+2/3\,e$, down-type quarks $-1/3\,e$ and neutrinos are uncharged. Besides their mass and charge, matter particles are also characterised by their half-integer spin. In addition to the particles in Figure 2.1, every particle has an antiparticle of opposite electric charge[1]. Despite this diversity, all elements in Mendeleev's Periodic Table are made up of electrons and up and down quarks, i.e. first generation particles. Particles of other generations and their composites are found in cosmic rays and they can be generated in particle accelerators.

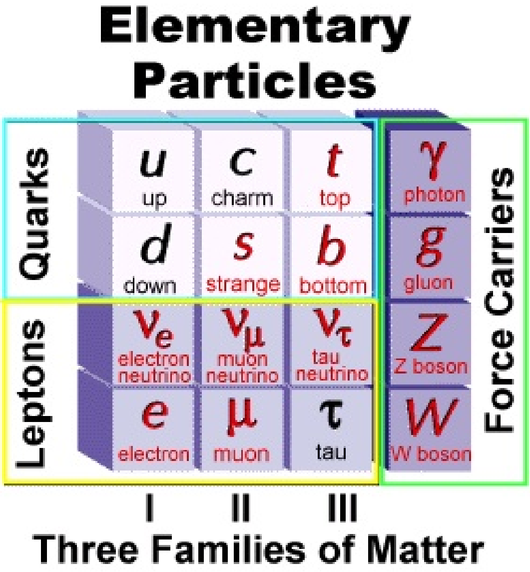

Figure 2.1: The elementary particles of the Standard Model (not including the Higgs boson).

In the SM there are three forces acting on the matter particles, each of them is transferred by so-called force-carrying particles. These bosons have integer spin. The electromagnetic force acts between electromagnetically charged particles and is transferred by the photon. The strong force only operates between colour-charged particles, i.e. quarks and their composites. There are three different colour charges, generally called 'red', 'green' and 'blue'. In nature one can only find colourless composites of quarks. These are called hadrons and can be subdivided into mesons, formed by combining a colour and its anticolour, and (anti)baryons, where the three (anti)colours are combined. Contrary to the photon, the force-

---

[1] It is not yet clear if the antineutrino is identical to the neutrino, cf. Majorana neutrinos [4], but it is certain that they have opposite chirality.

carrying particle of the strong force, the gluon, is charged itself—actually it is doubly charged, with one colour and one anticolour—, so both quarks and gluons are influenced by the strong force. (Composite) particles decay through the weak force, which is mediated by the charged W^+ and W^- bosons and the neutral Z boson.

A fourth force, gravity, is not included in the SM as a consistent quantum theory of gravity is yet to be developed. On the whole, gravity is supposed to be too weak to have a substantial influence in elementary particle physics. It is 40 orders of magnitude weaker than electromagnetism and about 10^{29} times weaker than the weak force [5].

One particle is missing in Figure 2.1. The elusive Higgs boson has only been discovered in 2012 and is responsible for giving mass to the other particles and itself [6–8]. It is also possible to introduce more complex Higgs mechanisms, which are generally needed in BSM-theories. These will result in more than one Higgs particle. The observed Higgs boson with a mass of about 126 GeV does not exclude a particular mechanism.

2.2 The Hierarchy Problem

The hierarchy problem arises from the radiative corrections to the Higgs boson mass. Most next-to-leading-order (NLO) processes cancel each other out, but one contribution remains. The relevant Feynman diagram is shown below.

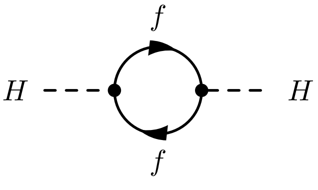

Figure 2.2: One-loop diagram contributing to the Higgs boson mass.

If the loop integral is cut off at a momentum scale Λ, the renormalised Higgs boson mass becomes

$$m_H^2 = \left(m_H^0\right)^2 + \frac{3\Lambda^2}{8\pi^2 v^2} \left(m_H^2 + 2m_{\mathrm{W}}^2 + m_{\mathrm{Z}}^2 - 4m_{\mathrm{t}}^2\right) , \tag{2.1}$$

where m_H^0 is the bare Higgs boson mass, m_{W} the mass of the W boson, m_{Z} the mass of the Z boson and m_{t} the mass of the top quark. The other quarks and leptons have such low masses that they will hardly contribute. The vacuum expectation value $v \simeq 246$ GeV is the average, expected value of the Higgs field in the vacuum.

The diagram in Figure 2.2 introduces a quadratic divergence into the renormalised Higgs boson mass when $\Lambda \to \infty$. If this term is to be neutralised, the Higgs boson mass must be tuned in order to cancel the contributions from the top quark and the W and Z bosons.

$$m_H^2 = 4m_{\mathrm{t}}^2 - 2m_{\mathrm{W}}^2 - m_{\mathrm{Z}}^2 \approx (320\,\mathrm{GeV})^2 \ . \tag{2.2}$$

If the SM is to be consistent, uniting the electroweak and the strong force, it must be valid up to the Grand Unification scale (GUT), i.e. $\Lambda \sim 10^{16}$. As $\Lambda^2 \sim (10^{16})^2 = 10^{32}$, the Higgs boson mass must be tuned to 32 decimal places. This unnatural tuning hints at the presence of new physics phenomena. The argument above can also be extended to radiative corrections of higher orders.

Introducing new particles can bring solace. As an example, the fermion sector will be worked out in more detail. The systematic cancellation of runaway divergences can only be the effect of a symmetry. This 'supersymmetry' (SUSY) will introduce a scalar partner for each fermion. The relevant one-loop diagrams are shown below, where ϕ_i are non-SM scalars.

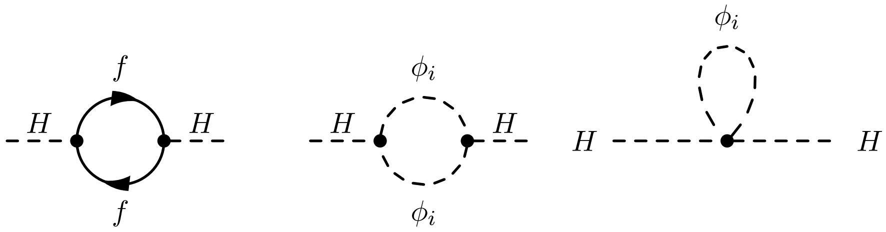

Figure 2.3: One-loop contributions to the Higgs boson mass.

The Yukawa coupling between the fermions and the Higgs boson is represented by the following term in the Lagrangian.

$$\begin{aligned}\mathcal{L}_{f\bar{f}H} &= -\lambda_f \bar{f}_L f_R H + \text{hermitian conjugate}\,,\\ &= -\frac{\lambda_f}{\sqrt{2}}\, f\bar{f}H - \frac{v\lambda_f}{\sqrt{2}}\, f\bar{f}\,,\end{aligned} \tag{2.3}$$

where f_L and f_R are the chiral components of the fermion and λ_f is its trilinear coupling. The last term of Equation (2.3) is equivalent to $-m_f f\bar{f}$, so the following relation between the fermion mass and the trilinear coupling is obtained,

$$m_f = \frac{v\lambda_f}{\sqrt{2}}\,. \tag{2.4}$$

If the external momentum of the Higgs boson is ignored, the correction term for the first diagram becomes

$$\left(\Delta m_H^2\right)_f = N_f\,\frac{\lambda_f^2}{8\pi^2}\,\left[-\Lambda^2 + 6m_f^2 \log\left(\frac{\Lambda}{m_f}\right) - 2m_f^2\right] + \mathcal{O}\left(\frac{1}{\Lambda^2}\right)\,, \tag{2.5}$$

where N_f is the number of fermions.

Assume there are N_s scalar particles with a mass m_s, trilinear couplings $v\lambda_s$ and quadrilinear couplings λ_s to the Higgs boson. Then,

$$\begin{aligned}\left(\Delta m_H^2\right)_s = {} & N_s \frac{\lambda_s}{16\pi^2}\left[-\Lambda^2 + 2m_s^2 \log\left(\frac{\Lambda}{m_s}\right)\right] \\ & + N_s \frac{v^2\lambda_s^2}{16\pi^2}\left[-1 + 2\log\left(\frac{\Lambda}{m_s}\right)\right] + \mathcal{O}\left(\frac{1}{\Lambda^2}\right) . \end{aligned} \tag{2.6}$$

If $\lambda_s = \lambda_f^2$ and $N_s = 2N_f$, then

$$\begin{aligned}\left(\Delta m_H^2\right)_s = {} & N_f \frac{\lambda_f^2}{8\pi^2}\left[-\Lambda^2 + 2m_s^2 \log\left(\frac{\Lambda}{m_s}\right)\right] \\ & + N_f \frac{v^2\lambda_f^4}{8\pi^2}\left[-1 + 2\log\left(\frac{\Lambda}{m_s}\right)\right] + \mathcal{O}\left(\frac{1}{\Lambda^2}\right) . \end{aligned} \tag{2.7}$$

The total correction term is the sum of Equations (2.5) and (2.7). Using Equation (2.4) to rewrite Equation (2.7), this becomes

$$\Delta m_H^2 = N_f \frac{\lambda_f^2}{4\pi^2}\left[(m_f^2 - m_s^2)\log\left(\frac{\Lambda}{m_s}\right) + 3m_f^2 \log\left(\frac{m_s}{m_f}\right) + m_f^2\right] . \tag{2.8}$$

The above correction term no longer contains quadratic divergences. There is still a logarithmic divergence, but even when $\Lambda \sim 10^{19}$ this term is quite small.

If SUSY is an exact symmetry, $m_s = m_f$, the logarithmic term disappears completely and the Higgs boson mass is no longer dependent on the energy scale. If SUSY is broken, the masses are no longer equal and the hierarchy problem returns when the difference between the masses is too large. In general, the theory remains stable when the scalars are of order 1 TeV.

Therefore, the hierarchy problem in the fermion sector is solved when, for each fermion, two scalar particles with couplings related to the SM couplings and a mass of order 1 TeV or lower are added. If these relatively light particles exist, they would come within the reach of currently existing experiments. The same argumentation can be followed for W and Z loops, thus introducing their superpartners.

2.3 Supersymmetry

In the past decades, the SM has been tested on many levels. Though experimental observations show great agreement with the theory, it remains insufficient to describe the entire universe. An extension to include other physical phenomena is required. Supersymmetry is an elegant way to provide more answers. The new symmetry introduces an operator that transforms a bosonic state into a fermionic state and vice versa, i.e.

$$Q\left|\text{boson}\right\rangle = \left|\text{fermion}\right\rangle , \qquad Q\left|\text{fermion}\right\rangle = \left|\text{boson}\right\rangle . \tag{2.9}$$

These superpartners are combined into a supermultiplet, or superfield, and have the same quantum numbers, except for their spin [1]. It are the superfields that will interact with each other, thus adding many new terms to the Lagrangian. As supersymmetry deals with transformations in superspace, space-time needs to be extended with new coordinates,

$$(x^\mu) \longrightarrow (x^\mu, \theta) \ , \tag{2.10}$$

where θ are Grassmann variables. These are subject to the Grassmann algebra and the interested reader can find their application to supersymmetry in [9].

As every SM particle gets a new partner, many new particles are added in SUSY and thus also many new parameters. If SUSY is an exact symmetry, the superpartners have the same mass as the SM particles. However, no evidence has been found of these new particles at the expected mass ranges. To allow for different masses, SUSY must be broken. Up till now there is no satisfactory way to accomplish this. So, instead of a fundamental mechanism, the SUSY breaking terms are added to the Lagrangian by hand.

2.3.1 The Minimal Supersymmetric Standard Model

In the minimal extension of the SM, the Minimal Supersymmetric Standard Model (MSSM), all SM leptons and quarks get scalar, spin-0 superpartners, called sleptons and squarks. The SM gauge bosons get spin-1/2 superpartners, the gauginos. Superparticles are indicated with a tilde, e.g. $\tilde{e}_L$ is the left-handed selectron, where the left-handedness refers to the chirality of its SM partner, since the selectron is a spin-0 particle. If lepton and baryon number are to be conserved, R-parity is imposed. This is a discrete and multiplicative symmetry and is defined as follows,

$$R = (-1)^{2S+3B+L} \ , \tag{2.11}$$

where S is the particle spin, B is the baryon number and L the lepton number. Every SM particle has a positive R-parity $R = +1$ and every supersymmetric particle has $R = -1$. As a consequence, supersymmetric particles can only be created in pairs and the lightest supersymmetric particle (LSP) is stable.

Once the desired components of the theory are determined, terms that yield this content are added to the Lagrangian. This is obtained from the superpotential that is constructed from the superfields [9]. The SUSY breaking terms consist of mass terms for the sfermions, gauginos and Higgs bosons and the trilinear couplings between the sfermions and the Higgs bosons. This way, 105 new parameters are added.

With a total of 124 parameters, phenomenological problems emerge. Some parts of the parameter space even yield unphysical results. To avoid this, the number of parameters will be reduced by imposing some assumptions. First of all, it will be assumed that the SUSY-breaking terms will not generate CP-violation, which implies that they are all real rather than complex [10]. Secondly, there are no flavour changing neutral currents at tree level, resulting in diagonal matrices for the sfermion masses and trilinear couplings. Thirdly, the masses and trilinear couplings of the first and second generation are presumed equal at low energy. This way only 22 SUSY parameters remain, whereof 10 sfermion masses, 6 trilinear couplings, 3 gaugino masses and 3 parameters related to the Higgs sector. The model thus generated is called the phenomenological MSSM (pMSSM).

2.3.2 The constrained MSSM

The parameter space of the pMSSM can be further constrained if one assumes a hidden sector in which the SUSY breaking occurs that can only interact with the visible sector through gravity. It is further assumed that these interactions are flavour blind. If there are universal conditions at the GUT scale ($\Lambda \sim 10^{16}$), the constrained MSSM (cMSSM) or minimal Supergravity model (mSUGRA) only contains 4 free parameters and 1 unknown sign,

$$m_0\,, \quad m_{1/2}\,, \quad A_0\,, \quad \tan\beta\,, \quad \mathrm{sign}\,\mu\,, \tag{2.12}$$

where m_0 is the universal scalar mass, $m_{1/2}$ the universal gaugino mass and A_0 the universal trilinear coupling. The parameters $\tan\beta$ and $\mathrm{sign}\,\mu$ originate from the Higgs sector. The vacuum expectation value of the Higgs boson introduces the parameter $\tan\beta$, whereas μ is a mixing parameter in the superpotential [9].

The original parameters can be obtained by evolving these 5 parameters from the GUT scale to the electroweak scale.

2.3.3 Simplified models

Models like the cMSSM bring the number of SUSY parameters to a manageable level, but they still predict certain mass patterns and signatures. This means that results obtained in the cMSSM mass plane $(m_0, m_{1/2})$ cannot be generalised to other MSSM models or extensions of these, as a variation of $A_0, \tan\beta$ and $\mathrm{sign}\,\mu$ does not reproduce the entire SUSY parameter space. Another approach, that does allow such a generalisation and can be used to place limits on different theoretical models, are simplified models. Here, a certain topological signature is generated by the introduction of a limited number of particles and their decay chains. For each simplified model, the masses of the particles involved are variable within a certain mass range. Examples of some common production processes can be found in Equation (2.13),

$$\begin{aligned} &\mathrm{q\bar{q}, gg} \to \mathrm{\tilde{g}\tilde{g}}\,, \qquad &&\mathrm{q\bar{q}, gg} \to \mathrm{\tilde{q}\bar{\tilde{q}}}\,, \\ &\mathrm{q\bar{q}, gg} \to \tilde{\chi}^0\tilde{\chi}^0\,, \qquad &&\mathrm{q\bar{q}, gg} \to \tilde{\chi}^0\tilde{\chi}^\pm\,, \end{aligned} \tag{2.13}$$

where $\mathrm{\tilde{g}}$ is a gluino, $\mathrm{\tilde{q}}$ a squark, $\tilde{\chi}^0$ a neutralino and $\tilde{\chi}^\pm$ a chargino. These can immediately decay into the LSP and SM particles or an intermediate particle can be formed. For example, a chargino can directly decay into a lepton, neutrino and neutralino, $\tilde{\chi}^{\pm} \to l\nu\tilde{\chi}^{0}$, or this final state can be produced by

$$\tilde{\chi}^{\pm} \to \mathrm{W}^{\pm}\,\tilde{\chi}^{0}\,, \quad \mathrm{W}^{\pm} \to l^{\pm}\,\nu\,, \tag{2.14}$$

$$\tilde{\chi}^{\pm} \to \tilde{l}^{\pm}\,\nu\,, \quad \tilde{l}^{\pm} \to l^{\pm}\,\tilde{\chi}^{0}\,, \tag{2.15}$$

$$\tilde{\chi}^{\pm} \to l^{\pm}\,\tilde{\nu}\,, \quad \tilde{\nu} \to \nu\,\tilde{\chi}^{0}\,. \tag{2.16}$$

In each of these cases, the kinematic properties of the lepton will be different, so a certain decay chain can be preferred over the other based on the aim of the analysis [11].

2.3.3.1 Direct stop quark pair production

A stop quark pair can be produced directly in collision experiments if the centre-of-mass energy is high enough. The squark[2] will then decay into a quark and the LSP or into a quark and an intermediate supersymmetric particle that, in its turn, decays to the LSP. If the LSP is a neutralino and the intermediate particle a chargino, this results in the following processes, which are also visualised in Figure 2.4,

$$\tilde{\mathrm{t}}\,\bar{\tilde{\mathrm{t}}} \to \mathrm{t}\,\tilde{\chi}^{0}\,\bar{\mathrm{t}}\,\tilde{\chi}^{0}\,, \tag{2.17}$$

$$\tilde{\mathrm{t}}\,\bar{\tilde{\mathrm{t}}} \to \mathrm{b}\,\tilde{\chi}^{+}\,\bar{\mathrm{b}}\,\tilde{\chi}^{-}\,, \quad \tilde{\chi}^{\pm} \to \mathrm{W}^{\pm}\,\tilde{\chi}^{0}\,. \tag{2.18}$$

Equation (2.17) represents direct stop decay into a top quark and a neutralino, while Equation (2.18) represents the decay via an intermediate particle. As the top quark decays into a bottom quark and a W boson, both processes have the same final state. This analysis will focus on the direct decay.

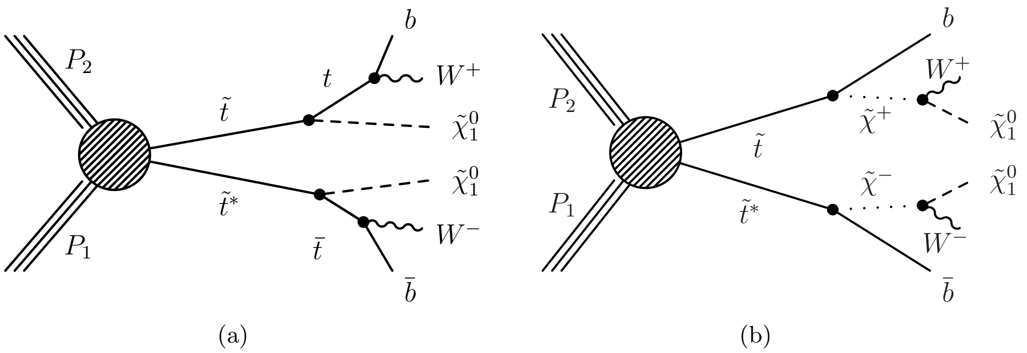

(a) (b)

Figure 2.4: Production of a stop quark pair, where each stop quark decays into a (a) top quark and neutralino (LSP); (b) bottom quark and chargino.

---

[2] Likewise for the antisquark.

2.3.3.2 State of the art

Relatively light stop quarks ($m_{\tilde{t}} < 1\,\mathrm{TeV}$) are a key object in solving the hierarchy problem, as the top quark is the heaviest SM particle and will thus contribute the most at one-loop level (see Equation (2.8)). Further, they are especially interesting because they should be observable at currently existing particle colliders.

Searches at centre-of-mass energies of 7 and 8 TeV are currently carried out by the ATLAS and CMS collaborations (see Chapter 3). So far, none has led to a discovery, but they do enable to reject a large part of the parameter space, specifically in the $(m_{\tilde{t}}, m_{\tilde{\chi}^0})$ mass plane. Figure 2.5 [12] shows the exclusion results from CMS for the $\tilde{t} \rightarrow t\tilde{\chi}^0$ channel, Figure 2.6 [13] shows the results from ATLAS for both decay channels mentioned in Section 2.3.3.1. The results were obtained using a multivariate analysis (MVA) technique.

As these techniques usually employ only part of the event information, the question arises if better results can be obtained if more information is used. The matrix element method, for example, uses all kinematic information present in the event and will be explored in Chapters 7 and 8.

This analysis will focus on investigating the performance of the matrix element method. To this purpose, one point in the $(m_{\tilde{t}}, m_{\tilde{\chi}^0})$ mass plane will be singled out, namely the one with $m_{\tilde{t}} = 350\,\mathrm{GeV}$ and $m_{\tilde{\chi}^0} = 100\,\mathrm{GeV}$, and tested. As can be seen from Figures 2.5 and 2.6, this parameter point is excluded by the ATLAS and CMS experiments. Therefore, it is expected to also exclude this point with the matrix element method. Once the procedure is set up, it can easily be repeated for other points in the parameter space.

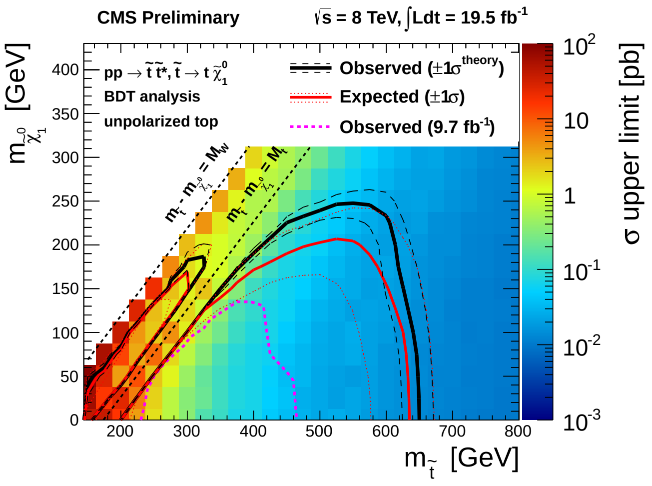

Figure 2.5: CMS exclusion contours for the $(m_{\tilde{t}}, m_{\tilde{\chi}^0})$ plane. The colour scale indicates the observed cross-section upper limit.

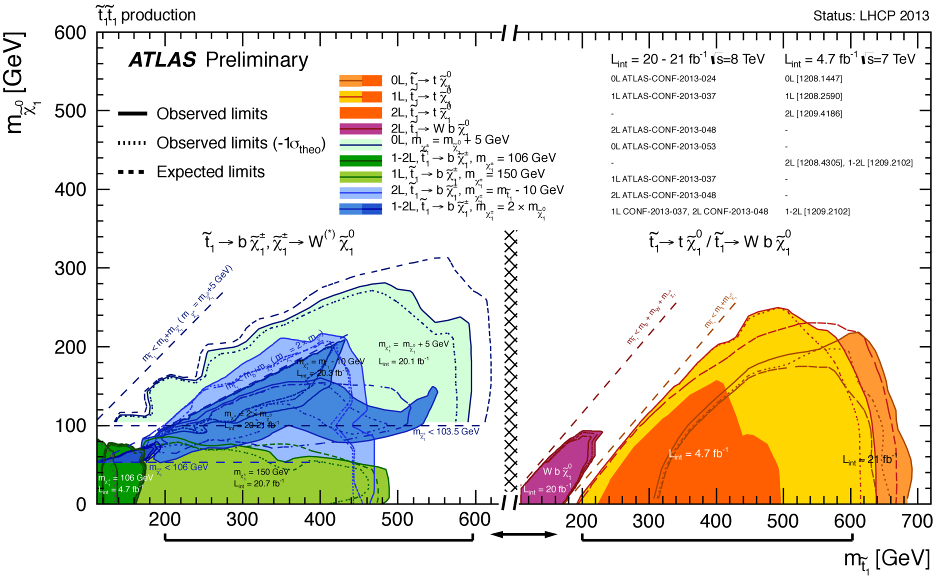

Figure 2.6: ATLAS summary plot for the excluded mass points in the $(m_{\tilde{t}}, m_{\tilde{\chi}^0})$ plane at 95% confidence level.

3

Observation of New Particles

Paradoxically, large instruments are necessary to investigate the minute particles appearing in the SM and BSM-theories. This is because the resolution of common microscopes is not good enough to discern them. In order to detect objects, the wavelength of the microscope needs to be smaller than the wavelength of the object. Elementary particles have a maximum size of about 10^{-18} m and an even smaller wavelength. Even the most precise microscopes do not meet those requirements. Therefore, colliders are needed to detect elementary particles. The particles are accelerated to a certain centre-of-mass energy before they collide into each other at the centre of a particle detector. The larger the centre-of-mass energy, the smaller scales the collider can probe. Colliders have the great advantage that the centre-of-mass energy is equal to the sum of the beam energies. This is not the case for a fixed target accelerator, where part of the energy is used to get the particles in the centre-of-mass frame.

When the accelerated particles collide, they produce new particles, the remnants of which are measured by the detector. Electrons and hadrons, in particular protons and ions, are the most commonly used accelerated particles. Each have their advantages and disadvantages. On the one hand, it is easier to accelerate hadrons to higher energies as they are not so prone to synchrotron radiation. When particles bend, they radiate away part of their energy. This is inversely proportional to their mass. As the electron is about 2000 times lighter than the smallest hadrons, the accelerator must provide more energy to electrons than to hadrons on curved tracks to make up for this energy loss. On the other hand, hadrons are composite particles. When they collide, it are their constituents that are involved in the actual collision. This means that, contrary to electron–positron collisions, the centre-of-mass energy is not known in hadron–(anti)hadron collisions. For these reasons, hadron colliders are most commonly used to make discoveries, while electron-positron colliders make precision measurements once the discovery has been made.

3.1 The Large Hadron Collider

The Large Hadron Collider (LHC), located at CERN at the Franco–Swiss border, is currently the most powerful particle accelerator in the world. It consists of eight sectors that are more or less straight, connected by eight arcs. The total circumference of the accelerator is approximately 27 km. Particles travel through the machine in two beam pipes, one in each direction. These are in an ultrahigh vacuum state to avoid collisions between the particles and air molecules. Dipole magnets are used to keep the particles in their orbit and quadrupole magnets focus them into collimated bunches of about 10^{11} particles. As these are accelerated to very high energies, the magnets need to be superconductive. They are cooled with liquid helium to 1.9 K. This way, the dipole magnets can produce a magnetic field of about 8.4 T [14].

Before being injected into the LHC, the hadrons are pre-accelerated. Protons are acquired by stripping electrons from hydrogen atoms and are accelerated to about 50 MeV by a linear accelerator. Then they are inserted into the PS Booster, where they get an energy of 1.4 GeV before being transferred to the Proton Synchrotron (PS), which further accelerates the protons to 25 GeV. In the Super Proton Synchrotron (SPS) this is upped to 450 GeV before the protons are finally inserted into the LHC. The accelerator complex is shown in Figure 3.1 [15].

Also lead ions can be accelerated in the LHC. The ions are first accelerated in the Low Energy Ion Ring (LEIR) before they are injected into the PS. Like the protons, they are then transferred to the SPS and the LHC.

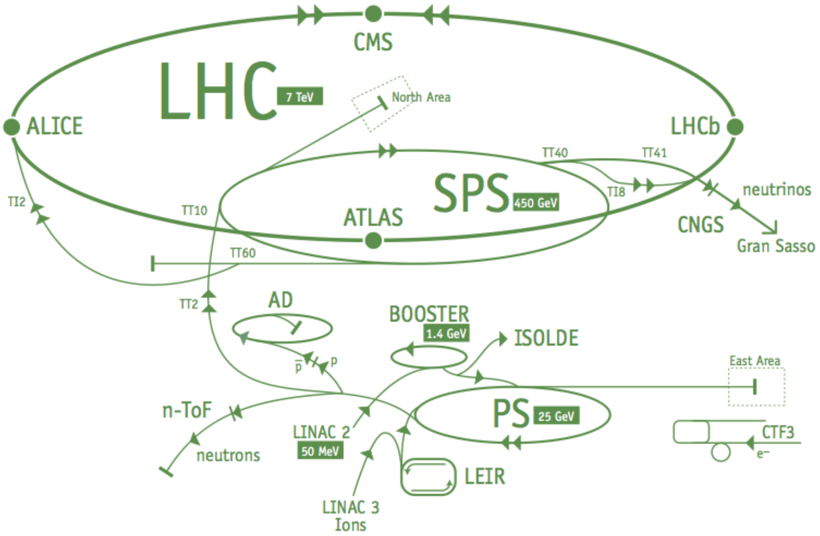

Figure 3.1: Schematic overview of the accelerator complex at CERN.

The LHC is designed to have a proton beam energy of 7 TeV, but due to technical problems only beam energies of 3.5 TeV (2011) and 4 TeV (2012) have currently been explored. This has proved to be sufficient for the discovery of the Higgs boson, which has a mass of about 126 GeV, but an upgrade to higher beam energies is favourable for the study of new physics, as the production cross sections of new physics processes increase more compared to those of the known processes. This upgrade will be carried out during the Long Shutdown (LS1) in 2013-2014.

The number of collisions in a certain time interval is defined by the luminosity,

$$\mathcal{L} = f n \frac{N^2}{A} \,, \tag{3.1}$$

where f is the revolution frequency, n the number of bunches, A the cross-sectional area of the bunch and N the number of particles per bunch. With about 2800 proton bunches and 10^{11} particles per bunch, the design luminosity of the LHC is $10^{34}\,\mathrm{cm}^{-2}\,\mathrm{s}^{-1}$ [16]. The integrated luminosity is obtained by integrating over time and is expressed in inverse barns, where $1\,\mathrm{b} = 10^{-24}\,\mathrm{cm}^2$.

Due to the collision of proton bunches instead of single protons, more than one interaction can occur during one bunch crossing. Particles belonging to different collisions are detected at the same time. This is called pile-up. If the particles cannot be traced back to their original collision, they can contaminate the energy measurement of others.

Along the accelerator line there are four major experiments to detect and investigate the remnants of the particle collisions when the two beams cross. These are called ALICE [17], ATLAS [18], CMS [19] and LHCb [20]. ATLAS and CMS are general-purpose detectors examining proton collisions. They are looking for new physics, but also investigate the SM more closely. The fact that there are two independent experiments is advantageous in the sense that one can always cross-check the results of the other. ALICE on the other hand looks at lead-ion collisions or the collisions between a lead ion and a proton to investigate quark–gluon plasma. This is expected to have been the state of the universe right after the Big Bang. LHCb looks for an answer to the matter-antimatter asymmetry in the universe. To this purpose it investigates CP-violation in b-quark physics.

Apart from these four, there are also some smaller experiments installed at the LHC. LHCf [21] is located near the ATLAS interaction point and TOTEM [22] resides near CMS. They focus on forward particles, which move close to the beam line.

This project will use proton collisions collected by the CMS experiment in 2012. In the next section, a description of the experiment and its components can be found. During its run time, the CMS experiment has collected about $5.32\,\mathrm{fb}^{-1}$ of data at a centre-of-mass energy of 7 TeV (2011) and $20.65\,\mathrm{fb}^{-1}$ at a centre-of-mass energy of 8 TeV (2012) [23].

3.2 The Compact Muon Solenoid Experiment

Each particle has intrinsic properties that make it easier or more difficult to detect with certain instruments. Therefore, the Compact Muon Solenoid (CMS) experiment is a multilayered structure, where each layer is dedicated to optimally recognise certain particle properties. The main component of the CMS detector is a powerful solenoid magnet that enables to distinguish the charges of particles. The magnet consists of a coil of superconducting cables, producing a magnetic field of 3.8 T [24]. It weighs about 12,000 tonnes and has a diameter of approximately 7 m, thus enveloping a silicon tracker, that is positioned at the heart of the detector, and an electromagnetic and a hadron calorimeter.

Outside the solenoid there are iron return yokes to close the magnetic field lines. These are interspersed with muon detectors. Muons[1] can traverse many meters of iron without interacting. In fact, they are the only particles that will reach this part of the detector—that is, not counting the neutrinos, which will not be detected. So as to be most effective to observe the muons, different kinds of muon detectors are used in different locations. As can be seen in Figure 3.2 [25], CMS is divided into a barrel region, which contains the solenoid, and two endcap regions. The endcaps are formed such that the CMS detector is almost hermetically sealed. This way, one can infer the presence of neutrinos, that will not be measured by any of the CMS components.

3.2.1 Coordinate system

The CMS detector is cylindrical in shape, so it would seem cylindrical coordinates present the easiest way to describe the positions of particles in the detector. The endcaps, however, do not have the same structure as the barrel region so as to optimally close the detector. In reality, this makes the usage of spherical coordinates more appropriate when the detector as a whole is considered. Figure 3.2 includes the cartesian coordinate system—which can easily be converted to spherical coordinates r, θ and ϕ—that is generally used. The z-axis lies along the beam pipe and the x-axis points towards the centre of the LHC ring. The xy-plane, or the plane defined by $\theta = \pi/2$, is also called the transverse plane. As protons are accelerated in the beam pipe, the total energy in the transverse plane is equal to zero before the collision. Since the conservation of energy dictates that the total transverse energy also needs to be zero after the collision, the transverse plane presents the ideal location to search for missing energy brought about by neutrinos or other elusive particles from BSM-models.

Instead of the spherical angle θ , collider physicists often use the pseudorapidity.

---

[1] In this section and the remainder of this thesis, the term ‘muon’ will be used to indicate both the muon itself and its antiparticle, unless it is explicitly specified. Likewise, the term ‘electron’ will indicate both the electron and the positron.

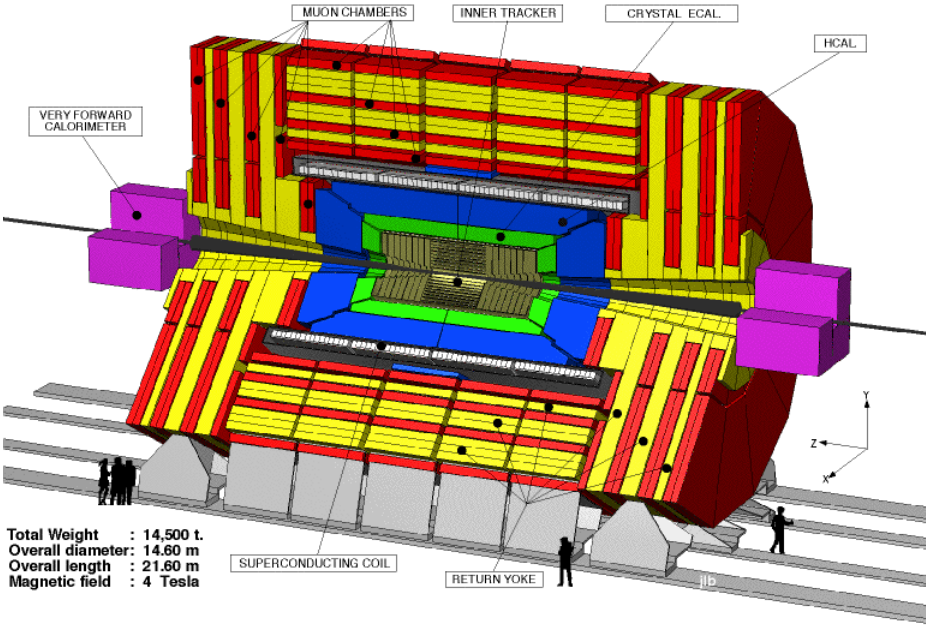

Figure 3.2: Schematic overview of the CMS experiment.

This is a Lorentz invariant quantity and is defined as

$$\eta = -\ln\left(\tan\frac{\theta}{2}\right). \tag{3.2}$$

This means that the transverse plane is located at $\eta = 0$ and the beam pipe at $\eta = \infty$.

3.2.2 The inner tracker

The interaction point in the centre of the CMS experiment is surrounded by a tracker, which consists of several layers of silicon detectors that will measure the position of charged particles. These charged particles will ionise some of the silicon atoms on their way, thus creating electron-hole pairs that will produce a small electrical signal. As the energy of the particles is supposed to be determined by the calorimeters beyond the tracker boundary, it is important that the particles are disturbed as little as possible. Apart from choosing a light material like silicon, this is realised by taking just a few measuring points that have a very high precision, in this case about 10 μm [26]. The magnetic field produced by the solenoid will bend charged particles into a curved track with radius

$$r = \frac{p_{\mathrm{T}}}{qB}, \tag{3.3}$$

where p_T is the transverse momentum, which is perpendicular to the magnetic field, q is its charge and $B = |\vec{B}|$ the magnitude of the magnetic field. Thus, combining the measurements, the helical track of the particles can be reconstructed and its momentum-to-charge ratio inferred. Since the tracker is the structure closest to the interaction point, it will receive the highest rates of particles. In addition to radiation hardness, the tracking detectors need to be very small to avoid occupancy problems. Closest to the interaction point, three concentric layers of silicon pixels, having a size of about $100 \times 150\,\mu\mathrm{m}^2$, are installed. These are followed by 10 layers of silicon strips of about $10\,\mathrm{cm} \times 80\,\mu\mathrm{m}$, up to $25\,\mathrm{cm} \times 180\,\mu\mathrm{m}$ at the outer edges of the tracker. In the endcaps there are two layers of silicon pixels and 11 layers of strips. This is visualised in Figure 3.3 [16].

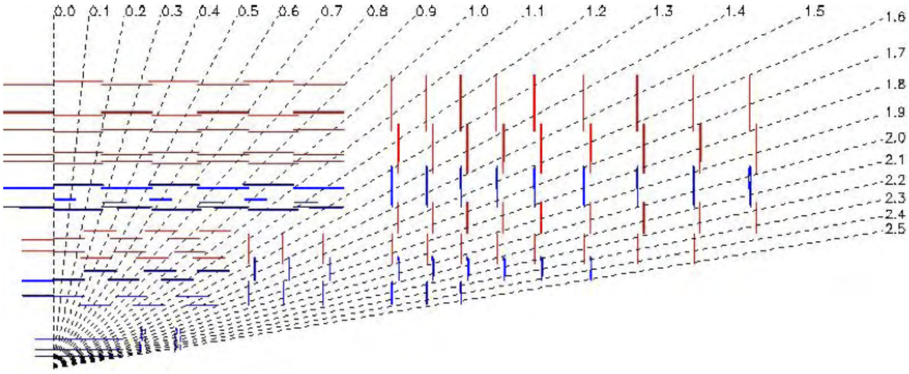

Figure 3.3: Layout of the tracker in one quarter of the CMS detector.

3.2.3 The calorimeter system

Calorimeters are used to determine the energy of particles. In order to do so, the calorimeter is composed of scintillating materials. These will produce a light pulse when a particle passes through it and excites the atoms in the material. Due to Stokes's shift [27], the light that gets produced when the atoms fall back to their ground state is not energetic enough to further excite atoms and the scintillating material will be transparent to the produced pulses. In the CMS experiment, two different scintillation techniques are used, each adapted to other types of particles. The crystalline structure of the electromagnetic calorimeter (ECAL) is ideal for determining the energy of electrons and photons. It is positioned between the central tracker and a hadron calorimeter (HCAL), that focusses on hadrons. The latter is a sampled detector. It consists of layers of absorbing material interleaved with tiles of scintillating plastic. When a particle hits the absorbing material, in this case brass or steel [28], a shower of secondary particles is produced. Every one of these can further produce a shower of its own. When the scintillating plastic is crossed by these particles, it emits high-frequency light of which the amount is proportional to the energy of the particle. Wavelength-shifting fibres convert this to greenish light, that is collected by optical fibres and sent to a readout box. The amount of light collected over the different layers of scintillating material is added to cover the track of the particle through the calorimeter and is a measure of its energy. The optical signals will be amplified in a proportional regime and converted to an electronic signal using hybrid photodiodes (HPD). These are designed especially for CMS and are constructed such that they can easily operate in places with strong magnetic fields [28,29].

The electromagnetic calorimeter consists of scintillating lead-tungstate ($PbWO_4$) crystals. These are very dense, which means that the ECAL is a remarkably compact structure. When an electron or photon enters the crystals, they will produce a shower of secondary electrons and photons. As in the HCAL, scintillation light proportional to the particles' energy will be produced. In the crystals, however, the amount of light that will be produced will also depend on the temperature. A precise cooling system is thus necessary to closely regulate the temperature of the crystals within 0.1°C [30]. In general, the light yield of the crystals will be low, so sensitive photodetectors are used to amplify the signal and convert it to electrical pulses. The photodetectors are glued to the back of the crystals and thus need to withstand strong magnetic fields and endure high radiation fluxes. In the barrel region, silicon avalanche photodiodes (APD) will be used. As the radiation flux in the endcap regions is too high for silicon photodiodes, vacuum phototriodes (VPT) will be employed there [30,31].

The granularity of the ECAL is about 25 times larger than that of the HCAL. Therefore, the amount of energy deposited is more precisely determined for electrons and photons than for hadrons.

3.2.4 The muon system

Muons will be observed using gaseous detectors like drift tubes (DT), cathode strip chambers (CSC) and resistive plate chambers (RPC). In the barrel region DTs and RPCs are installed. These are visualised in Figure 3.4. RPCs consist of two parallel plates of high resistivity separated by a gas gap. The uniformity of the gap is ensured by introducing spacers. A voltage difference between the plates creates an electric field in the gap that is suitable for electron multiplication. When a charged particle like a muon enters the gap, it ionises the gas and the electrons snowball into an avalanche. This is read out by an external readout system, as the, for CMS, bakelite plates are transparent to the electron signal. CMS uses double-gap RPCs with a common readout system, as can be seen in Figure 3.4(a). The copper readout strips are positioned such that a quick momentum estimate can be made. RPCs have a good spatial resolution and an excellent time resolution of about 1 ns. As a result, they also have good rate capabilities [32,33].

DTs are especially good at determining the position of passing muons. They are about 4 cm wide and have an anode wire in the middle. Whenever a muon runs through it, the gas inside the DT gets ionised. The electrons will then drift to the anode and the position of the ionising particle can be inferred from where

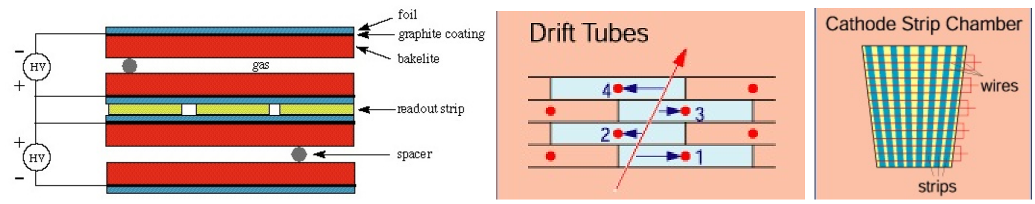

(a) RPC [34] (b) DT [35] (c) CSC [36]

Figure 3.4: Muon detectors at the CMS experiment.

the electrons hit the wire and the time it takes them to reach it. There are four layers of DTs, which are two by two orientated in another direction. This way, two coordinates can be determined at once [35]. Unfortunately, DTs have very poor rate capabilities. Therefore, the endcaps, where the rates are high and the magnetic field is uneven, employ CSCs instead of DTs [36]. Apart from anode wires, CSCs also have cathode strips that run perpendicular[2] to them. As always, the electrons that stem from the ionisation of the gas will drift to the anode wires. At the same time, the cathode strips will attract the ionised atoms. Hence two coordinates can be read out at once. To accurately identify the muons, there are 6 CSCs in each module.

3.3 Trigger and Data Aquisition

The LHC produces roughly one billion proton collisions per second. This corresponds to about 40 MHz of data. It is clear that only a small fraction of this can be stored on disk. As there are only 25 ns between bunch crossings, the decision on whether an event is interesting enough to keep needs to be made quickly. This decision-making will occur in two steps. After each bunch crossing, the events are placed in a pipeline for a maximum of 3.2 μs. The Level-1 (L1) trigger will reduce the event rate to 100 kHz. To this purpose, it uses simple, hardcoded algorithms. Despite being placed close to the detector, about 2 μs will be spent transporting the electrical signals, leaving only 1 μs to make the actual decision. Therefore, the L1 will only use macrogranular calorimeter and muon system information. The events that passed the L1 will then be built by the data aquisition system (DAQ) using a fast switch network [37]. This will be used as input for the high-level trigger (HLT), which will further reduce the event rate to 10^2 Hz.

---

[2] In fact, all cathode strips run towards the beam pipe. As a result, the strip spacing gets smaller the closer they are to the beam pipe. The anode wires thus run perpendicular to the strips in the centre of the CSC chamber.

4

Reconstruction of Particles

When particles move through the CMS detector, they leave electronic signals in its subdetectors that are not easily interpretable. A combination of these signals into particle tracks or energy deposits is a lot more intelligible. The particle flow algorithm [38] will combine the information from all subdetectors to accurately reconstruct and identify each stable particle. These will then be used to build jets, reconstruct tau leptons and determine the missing transverse energy $\not{E}_{\mathrm{T}}$.

Section 4.1 will describe how particles are identified, merging the information from the subdetectors. Section 4.2 shows how electronic signals are combined to reconstruct tracks and calorimeter clusters, while Section 4.3 joins this information to make fully reconstructed 'particle flow muons' and 'particle flow jets'.

4.1 Identification of Particles

When two protons collide in the centre of the CMS detector, particle debris will fly in all directions and leave behind signals when it crosses the detector. Combining the information from the subdetectors, an identification of the particles in question can be made. Figure 4.1 [39] shows a transverse slice of the detector where the signals of some particles are indicated.

Muons will leave a signal in the inner tracker, the calorimeters and in the muon chambers. Due to the position of the solenoid, the direction of the curvature will be reversed in the muon chambers compared to the tracker. The amount of energy deposited in the calorimeters is typically small.

Electrons, on the other hand, will deposit all their energy in the calorimeters, as will other charged particles. They leave a track in the inner tracker and the position of the energy deposit depends on the nature of the particle. Electrons will deposit most of their energy in the electromagnetic calorimeter, while for hadrons the deposit will be the largest in the hadron calorimeter.

Neutral particles will behave likewise in the calorimeters, but they will not leave a track in the inner tracker, as they cannot create electron-hole pairs. While

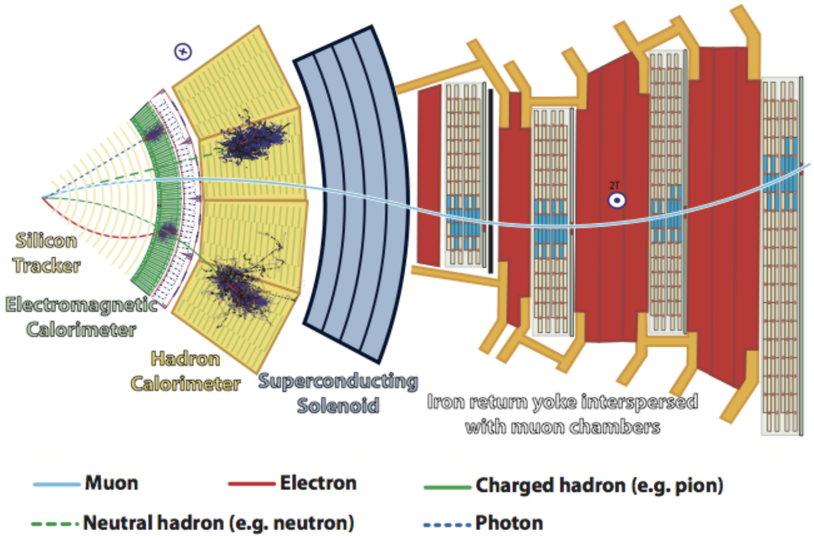

Figure 4.1: Interactions of particles in the CMS detector.

photons are reconstructed with an excellent energy resolution due to the high granularity of the electromagnetic calorimeter, neutral hadrons with a $p_{\mathrm{T}} \sim 100\,\mathrm{GeV}$ generally have a resolution of about 10% in the combined ECAL and HCAL system [38]. Therefore, they are solely perceived as an energy excess on top of the energy deposited by charged hadrons, which are also reconstructed by the tracker. If a neutral particle decays into charged particles while it is still in the inner tracker, the tracks from its decay products will originate from a vertex that is displaced compared to the interaction point.

Heavy particles, like tau leptons and top quarks, will decay before they can leave a track or deposit energy. They will be reconstructed using the signals of the particles in which they decay. Therefore, a good theoretical knowledge of the decay chain is necessary. As it is not trivial to indicate parent particles with confidence, this will be intensively simulated.

Neutrinos are the only SM particles that will not leave a signal in any of the subdetectors. Their presence will be inferred from missing energy in the transverse plane.

4.2 Object Reconstruction in the Subdetectors

4.2.1 Track reconstruction in the inner tracker

The layered structure of the tracker, see also Figure 3.3, facilitates the reconstruction of tracks. Moreover, the almost constant magnetic field in the largest part of the tracker allows for the application of a simple helical track model. The reconstruction speed can further be optimised if the tracker material is attributed to the layers instead of including a detailed distribution. Thus no additional steps will be necessary to include multiple scattering and energy losses due to ionisation and Bremsstrahlung [40].

The reconstruction of a track starts from a seed that is generally composed of hits in the first two pixel layers [41]. Starting from a rough estimate of the track parameters, the seed is iteratively expanded to the next layer, which increases the precision of the parameters. One of the most time-consuming parts of the track fit is to find the detectors that most probably contain the next hit, also called navigation. This is largely solved by organising the detectors in a (quasi-)periodic way. In the transition region between the barrel and the endcaps, however, navigation will still play an important role as more than one layer can be the next due to the difficult geometry. Often several hits on the next layer are compatible with the seed. The trajectory through each of these hits will be calculated and given a weight based on their respective uncertainties. Sometimes a particle will not interact with all layers on its way through the tracker. To keep these 'invalid hits' into account, a trajectory where there was no hit in the next layer will be calculated in addition to those with a compatible hit [40]. All these trajectories will be expanded to the next layer. However, if the uncertainty on the track parameters is large, the seed will be compatible with many nearby hits. To avoid an exponential increase of track candidates, a cutoff on the χ^2 value of the trajectory will be applied.

Once the track candidates are fitted, one trajectory is chosen as the reconstructed track. Therefore, the fraction of shared hits between two trajectories is determined,

$$f_{\text{shared}} = \frac{N^{\text{hits}}_{\text{shared}}}{\min\left(N^{\text{hits}}_1, N^{\text{hits}}_2\right)}\,, \tag{4.1}$$

where N_i^{hits} is the number of hits of the i^{th} trajectory. If $f_{\text{shared}} > 0.5$, the trajectory with the least number of hits is discarded. If the trajectories have the same number of hits, the one with the highest χ^2 value will be discarded [40]. This ambiguity resolving technique will be applied on all track candidates resulting from one seed, but also on the complete set of tracks that is produced by all the seeds, in case different seeds give the same track.

As the complete information about the track is only available at the last hit in the trajectory, the track will be refitted with a least squares method. More specifically, a combination of a standard Kalman filter and a smoothing algorithm will be implemented [42]. First, the Kalman filter will be initialised at the most central hit with estimates for the track parameters obtained during seeding. The corresponding covariance matrix, though, will be scaled with a large factor to avoid bias. In the iterative fit, the position estimate will be re-evaluated for each hit using the current values of the track parameters. These will then be updated, together with the covariance matrix. A second, 'smoothing' filter will work outside-in. It will start with the final value of the first filter, the covariance matrix again scaled with a large factor, and run back towards the centre of the tracker. At each hit, the updated parameters of the second filter, containing the information from the outermost hit up to—and including—the current hit, will be combined with the parameters obtained with the first filter, containing the information from the innermost hit up to—and not including—the current hit. This will give optimal estimates of the parameter values associated with each hit. The effectiveness of this technique will especially be visible at the first and last hit of the trajectory [40].

An iterated fit with relaxed constraints on the origin vertex also allows for the reconstruction of secondary particles. Only three hits, a p_{T} larger than 150 GeV and a vertex located maximally 50 cm from the beam axis are necessary to reconstruct charged particles with a fake rate of the order of 1% [38].

4.2.2 Reconstruction of energy deposits in the calorimeters

The clustering of energy deposits will occur independently in the barrel and in the endcaps. Calorimeter cells containing an energy that is larger than a certain energy value, which depends on the location of the cell in the calorimeter system, will act as seeds. Topological clusters are formed by aggregating neighbouring cells that have an energy that is at least two standard deviations higher than the electronic noise [38].

Apart from detecting and measuring the energy and direction of neutral particles, which do not leave a track, calorimeter clusters can also separate these neutral hadrons from charged ones, reconstruct and identify electrons and help with the energy measurement of charged hadrons with low-quality, or high-p_{T} tracks.

4.2.3 Track reconstruction in the muon system

Track fitting in the muon system is also based on a Kalman filter. A generic interface that is also shared with the inner tracker makes sure that it is not important which subdetector recorded the measurements. The tracker and the muon system can thus use the same tracking tools and track parametrisation [43]. First, a seed is defined by searching for patterns in the DT and CSC stations, using rough geometrical criteria. Assuming the muon is produced at the interaction point, an estimate of the transverse momentum p_{T} can be made. Then the seed is propagated inside-out to refine the seed and get a first estimate of the track parameters. Afterwards, the trajectory is built outside-in. As before, the iterative algorithm to do so will search the next compatible layer and propagate the track parameters. The best measurement is found using a χ^2 technique and the track parameters are updated with the information from the measurement if the χ^2 value complies with the cutoff criterion.

A trajectory will only be accepted as a muon track when there are at least two hits in the fit, whereof at least one is produced in the DT or CSC stations. This way, fake tracks due to combinatorics are rejected [43].

In the final step, the trajectory is extrapolated to the beam line. A constraint on the maximum distance from the interaction point will improve the momentum resolution.

4.3 The Particle Flow Algorithm

Particles that are the easiest to identify will be the first to be reconstructed. As all tracks in the muon system specifically indicate the presence of one particle, the particle flow (PF) algorithm will start with the reconstruction of muons (see Section 4.3.1). Then, electrons, characterised by their short track that clearly indicates the Bremsstrahlung energy loss, are reconstructed. The tracker being much more precise than the calorimeters, charged hadrons will be next in line. Excluding the muon and electron tracks, the remaining tracks have to comply with strict criteria in order to minimise the number of fake tracks. If the relative uncertainty on the p_{T} has to be smaller than the average relative energy resolution for charged hadrons, about 0.2% of tracks get rejected. About 10% of these originate from real particles, but they can still be measured with more precision in the calorimeters [38]. A rough estimate of the expected energy can be made if it is assumed that the mass of the hadron is about equal to the charged pion mass. If an excess energy is found in the calorimeters, photons and neutral hadrons are identified, depending on the location of the offset. In general, photons are more prevalent than neutral hadrons [38].

Tau leptons decay hadronically in two out of three cases, most often into one or three charged hadrons. The PF algorithm will first measure the energy and direction of its decay products (see above) and then make a reconstruction of the tau lepton in a cone with $\Delta R = 0.15$ around the leading particle.

When the event has been reconstructed, the PF algorithm allows an easy determination of the missing transverse energy. The transverse momentum of the reconstructed particles is summed vectorially and reversed. The modulus of this vector constitutes the missing transverse energy.

The results of the commissioning of the algorithm, using events with a centre-of-mass energy of 0.9 to 2.36 GeV, can be found at [44].

4.3.1 Muon reconstruction

A global muon track is retrieved when the muon track in the inner tracker, or tracker track, is connected with the so-called stand-alone muon track originating from the muon system. As the multiplicity of tracker tracks is large, a subset of tracks will selected that roughly correspond to the stand-alone muon track in momentum and position. This subset will be iterated over, ever increasing the strictness of the spatial and momentum matching conditions in order to select the best tracker track. Then a global refit of the silicon and muon hits will be done to make a new global track. If there are several possibilities, the global muon track with the least χ^2 value is chosen. This ensures that there is only one global muon track for each stand-alone muon track [43].

There are some cases in which the combination of the tracker track and the entire stand-alone muon track is not advantageous. High energy muons—several hundreds of GeVs or more—can suffer large energy losses in the production of electromagnetic showers in the iron return yokes. Not only does this alter the curvature of the muon's track, the shower can also contaminate the following muon detectors, producing false hits. To minimise these effects, the global muon track will be fitted multiple times with different sets of hits. For example, the First Muon Station algorithm will fit the tracker hits and the hits of the first muon station, while the Picky Muon Reconstructor will apply tighter cuts to the compatibility of new hits to the trajectory in muon stations with a high multiplicity of hits. A goodness-of-fit test will then evaluate the different trajectories.

On the other hand, muons having a p_T lower than 10 GeV often do not leave enough hits in the muon system to enable a full stand-alone muon track reconstruction. To identify them, all tracker tracks are considered and signals in the calorimeters and muon system are checked for their compatibility. The connection between the tracker tracks and the muon system hits is deliberately kept very loose in the search for these 'tracker muons', so they should not be used without further requirements [43].

In general, the tracks of low energy muons, that is, with $p_\mathrm{T} < 200\,\mathrm{GeV}$, in the muon system are dominated by multiple scattering.

Apart from being created directly, in the decay of heavy particles like W and Z bosons, muons can also be produced by the decay of B and D hadrons in jets (see Section 4.3.3). As the latter are just a by-product, it is important to be able to differentiate them from muons produced at the primary vertex. Muons produced in jets are usually surrounded by a multitude of particles, thus a relative isolation variable can do the trick. To determine this isolation variable, a virtual cone with an opening angle of 0.3 is drawn around the muon. Then,

$$\mathrm{relIso} = \frac{p_\mathrm{T}(CH) + \max\left[0\,,\, p_\mathrm{T}(NH) + p_\mathrm{T}(\gamma) - 0.5\, p_\mathrm{T}(puCH)\right]}{p_\mathrm{T}(\mu)}\,, \tag{4.2}$$

where CH indicates the contributions from charged hadrons within the cone, NH the contributions of neutral hadrons and $puCH$ the charged hadron contributions originating from pile-up. This is visualised in Figure 4.2 [16]. The muon is said to be isolated if the relative isolation value is smaller than 0.12.

4.3.2 Electron reconstruction

Electron reconstruction starts with the reconstruction of energy clusters in the ECAL. These cluster seeds are expanded to superclusters by taking a window around the seed to include Bremsstrahlung photons. The position of the supercluster is then used to predict the position of the electron hits in the first layers of the inner tracker. These hits usually serve as seeds for the track reconstruction [41] and, as the majority of the tracker material is still to come, most electrons have not yet radiated significantly at this point. To keep this energy loss into account, a dedicated electron tracking procedure with a looser χ^2 and a higher p_T cut will

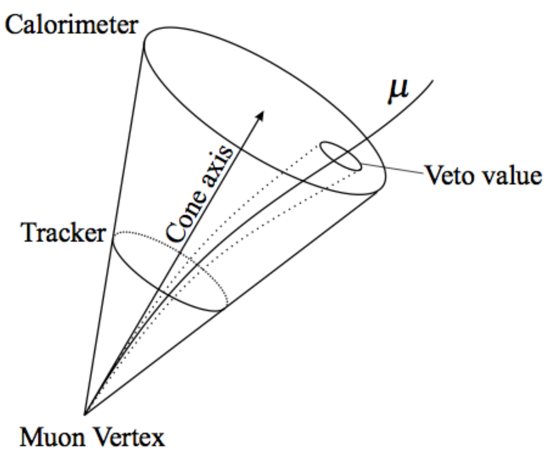

Figure 4.2: Muon isolation cone. The veto cone allows to differentiate the contribution of the muon from those of other particles within the cone.

be implemented. This procedure will use a Gaussian-sum filter to estimate the electron track parameters at each measuring point [45]. The difference in transverse momentum between the outermost and the innermost track position gives an estimate of the fraction of energy that is radiated away [46].

This technique is very efficient for electrons with a $p_{\mathrm{T}} > 5\,\mathrm{GeV}$ and for isolated electrons, having a relIso smaller than 0.1. It is not ideal for electrons present in jets, because superclusters might also include contributions from neutral particles. There is also a tracker driven reconstruction approach, where seeds are built from general tracks and then matched with clusters in the calorimeter [47], that is better suited for this case.

4.3.3 Jet reconstruction

Hadrons arise when quarks produced in proton collisions fragment and hadronise. To reconstruct the properties of the original quark, the hadrons need to be clustered in jets. To this purpose, CMS will use the anti-k_{T} algorithm with $R = 0.5$. On top of being infrared- and collinear-safe (IRC, see Appendix A) and simple to implement, it is also soft-resilient. This means that the shape of the jets is not influenced by soft radiation, thus simplifying theoretical calculations and facilitating the experimental calibration of jets [48].

The algorithm defines some interparticle distances d_{ij} and distances between particles and the beam axis d_{iB},

$$\begin{aligned} d_{iB} &= p_{\mathrm{T},i}^{-2}\,, \\ d_{ij} &= \min\left(p_{\mathrm{T},i}^{-2}, p_{\mathrm{T},j}^{-2}\right)\frac{\Delta_{ij}^2}{R^2}\,, \qquad \Delta_{ij}^2 = (y_i - y_j)^2 + (\phi_i - \phi_j)^2\,, \end{aligned} \tag{4.3}$$

where R is a distance parameter, ϕ_i the azimuthal angle and $y_i \equiv \frac{1}{2}\ln\frac{E+p_z}{E-p_z}$ the rapidity of particle i. These distances are determined for all particles. If a d_{ij} is the smallest distance, particles i and j will be combined to a 'pseudojet'. When a D_{iB} is the smallest jet, particle/pseudojet i is called a jet and will be removed from the list of particles. Other jet clustering algorithms are explained in Appendix A.

When there is only one hard particle and several soft particles, the soft particles will first cluster around the hard particle before clustering amongst themselves. This is a direct consequence of the inverse p_T in the distance definition.

Soft particles do not change the shape of jets, hard ones, on the other hand, do. When there is another hard particle within $2R$ of the first, but farther than R, two hard jets will be created. If $p_{\mathrm{T},1} \gg p_{\mathrm{T},2}$, the first jet will be conical and the second one will be partly conical, missing the overlap, which is attributed to the first jet. If the transverse momenta are about equal, the overlap will be divided over the two jets. When two hard particles are within R from each other, only one jet will be formed.

4.3.3.1 Identification of b jets

Jets originating from a b quark have some properties that allow them to be differentiated from other jets. b quarks often hadronise into B hadrons, which have a considerable lifetime [3]. Contrary to lighter hadrons, they still decay in the tracker and hence produce a secondary vertex (SV). A SV is only designated as such when it shares less than 65% of its associated tracks with the primary vertex (PV) and its flight direction is within a cone of $R = 0.5$ around the jet direction. If the radial distance to the PV is longer than 2.5 cm or if its mass is larger than 6.5 GeV, the SV candidate is rejected to avoid selecting vertices resulting from interactions with the detector material or decays of long-lived mesons [49].

Simple algorithms use only one observable, like the flight distance, to tag b jets. Others combine several observables to increase the discriminating power. CMS uses the Combined Secondary Vertex algorithm, or CSV. Contrary to simple secondary vertex algorithms, it also allows for a b jet identification when no SV can be fitted, thus increasing the efficiency. Since D hadrons have a non-negligible lifetime, though to a lesser extent than B hadrons, the differentiation between b and c jets is more challenging than their distinction from light jets (u, d, s and jets originating from gluons).

b-tag algorithms return a discriminator value for each jet. Depending on the physics analysis, a minimum threshold is applied to identify a jet as originating from a b quark and to limit the amount of misidentifications [49]. Different working points are defined according to the purity that is required. A loose cut permits a mistagging rate of about 10% at p_T values of 80 GeV, while this is about 1% for a medium cut and about 0.1% for a tight one. The working point of an analysis is indicated by appending an identifying letter to the algorithm name. For this analysis the CSVM tagger will be used.

4.3.3.2 Removal of isolated leptons

As mentioned before, several hadrons also have leptonic decay modes, making the presence of leptons in jets not unusual. It is important, though, to exclude isolated leptons that accidentally end up in the jet. Therefore, relative isolation cuts will be applied to the leptons. All muons with a relIso < 0.2 and all electrons with relIso < 0.15 will be excluded from the jets. These cuts are stricter than those in Sections 4.3.1 and 4.3.2 to avoid that isolated leptons would be reconstructed as jets.

5

Event Selection

5.1 Event Topology

This analysis will consider stop quark pair production, where a stop quark decays into a top quark and a neutralino, which is the LSP in this simplified model. A stop quark mass of 350 GeV and a neutralino mass of 100 GeV are assumed. This process is depicted in Figure 5.1(a). In many ways the process looks like an ‘ordinary’ pp → $t\bar{t}$ process, which is visualised in Figure 5.1(b), but there are some important differences. First of all, the stop quark decays into a top quark and a neutralino, which will not be detected by the CMS detector. This will manifest itself in a higher missing transverse energy compared to the missing transverse energy in $t\bar{t}$ processes. Secondly, the stop quark is heavier than the top quark, which implies that its decay products will have a larger transverse momentum than those of a top quark.

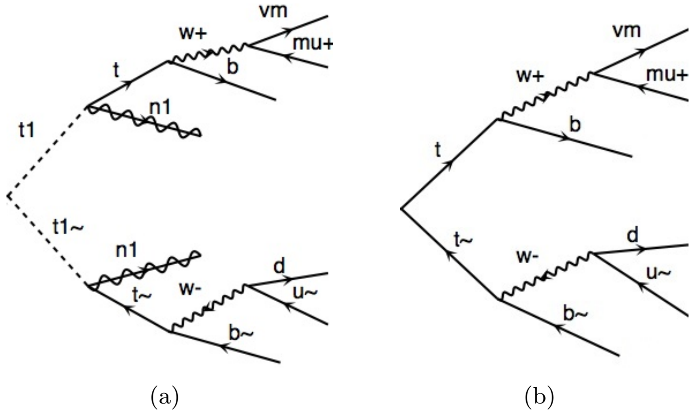

(a) (b)

Figure 5.1: Topology of the semi-muonic decay of a (a) stop quark pair; (b) top quark pair. Antiparticles are indicated with a tilde.

The top quark decays almost 100% into a bottom quark and a W boson. The latter will decay into a quark pair or into a charged lepton and its corresponding neutrino. The probability for a given particle to decay into a set of other particles is called the branching ratio (BR). For the W boson these are approximately [3]

$$\mathrm{BR}(\mathrm{W} \rightarrow q\,\bar{q}) \approx 2/3 \ , \qquad \mathrm{BR}(\mathrm{W} \rightarrow l\,\nu_l) \approx 1/3 \ . \tag{5.1}$$

The decays of (s)top quark pairs can thus be categorised into fully hadronic decays, where both W bosons decay hadronically, fully leptonic decays, where both W bosons decay leptonically, and semi-leptonic decays, where one W boson decays into a quark pair and the other into a lepton and a neutrino. This analysis will focus on semi-leptonic decays where the lepton is a muon. Being easily recognisable in the CMS detector, the muon offers a fine trigger. At the same time, the hadronic decay still allows a full mass reconstruction of the W boson and the top quark. The BR for a semi-muonically decaying top quark pair is

$$\begin{aligned}
\mathrm{BR}(\mathrm{t}\,\bar{\mathrm{t}} \rightarrow \mathrm{b\,q\,\bar{q}\,b}\,\mu\,\nu) = {} & \mathrm{BR}(\mathrm{t} \rightarrow \mathrm{b\,W}^{+}) \cdot \mathrm{BR}(\bar{\mathrm{t}} \rightarrow \bar{\mathrm{b}}\,\mathrm{W}^{-}) \\
& \cdot \big[\mathrm{BR}(\mathrm{W}^{+} \rightarrow \mathrm{q\,\bar{q}}) \cdot \mathrm{BR}(\mathrm{W}^{-} \rightarrow l\,\bar{\nu}) \cdot P(l = \mu) \\
& \quad + \mathrm{BR}(\mathrm{W}^{+} \rightarrow \bar{l}\,\nu) \cdot P(l = \mu) \cdot \mathrm{BR}(\mathrm{W}^{-} \rightarrow \mathrm{q\,\bar{q}})\big] \\
\approx {} & 4/27 \ ,
\end{aligned} \tag{5.2}$$

where $BR(\mathrm{t} \rightarrow \mathrm{b\,W}) \approx 1$ and the probability that a lepton is a muon is $1/3$.

As the stop quark has not yet been observed, it is not clear what its branching ratio to a top quark and a neutralino is. In this analysis, it is assumed to be one.

The amount of produced stop quark pairs depends on the cross section of the process and the integrated luminosity. At a centre-of-mass energy of 8 TeV, the cross section times BR is equal to 180.85 fb. As a comparison, the cross section for a semi-muonically decaying $\mathrm{t\bar{t}}$ process is 33.363 pb. The CMS experiment collected about 19.1 fb^{-1} of well-reconstructed proton collisions at 8 TeV. This results in about 638073 $\mathrm{t\bar{t}}$ events compared to only 3459 $\tilde{\mathrm{t}}\bar{\tilde{\mathrm{t}}}$ events. If only this $\mathrm{t\bar{t}}$ process is considered as background, this corresponds to a signal-to-background ratio S/B of only 0.5%! So, apart from selecting events with the correct final state, additional event selection requirements are needed to increase the signal-to-background ratio.

5.2 Event Generation and Simulation

As can be seen in Figure 5.1, the signature of the signal events, i.e. four jets, a muon and missing transverse energy, can also be produced by other processes. These constitute the background of the analysis. The main background processes are $\mathrm{t\bar{t}}$, single top, W+jets, Z+jets and QCD multi-jet events.

A Monte Carlo (MC) simulation is made of the background and signal samples in order to model the events that will meet the selection criteria specified in the next section. The signal sample and most of the background samples were simulated with `MadGraph/MadEvent` [50]. The single-top samples were simulated with `POWHEG` [51–53]. `PYTHIA` [54] was used to simulate initial and final state radiation and the showering of quarks, using a perturbative model for the fragmentation and the Lund model [55] for the hadronisation.

Besides simulating the signal and background processes, also a simulation of the detector was made. As the detector is granular, it is possible that some particles avoid detection by escaping through the cracks. Also interactions with the detector material can obscure the original event. The used materials and the geometry of the detector were simulated with `GEANT4` [56, 57].

Top quark pairs

The largest background contribution will come from the semi-leptonic decay channel where the lepton is a muon (see Fig. 5.1(b)), but other decay channels will also have an influence. For example, $t\bar{t}$ processes without direct muon production, where a tau decays into a muon, doubly-leptonic decays where the second muon is not observed and fully hadronic decays where a non-isolated muon is identified as isolated.

Considering a top quark mass of 173 GeV, the NLO cross section for $t\bar{t}$ processes is 225.2 pb [58]. A sample was simulated corresponding to an integrated luminosity of about $30\,\mathrm{fb}^{-1}$.

Single top (ST)

Top quarks are also produced singly, either in association with another quark or with a W boson. Especially the tW channel will contribute to the background as only one additional jet is needed to get the desired final state.

For a top quark mass of 173 GeV, the approximate NNLO cross section of the tW channel is about 22.2 pb and about 87.1 pb for the t channel [58]. The s channel is not considered in this analysis, because, due to the small production cross section, no events will pass the selection requirements.

The integrated luminosity is about $62\,\mathrm{fb}^{-1}$ for the simulated t channel sample and about $44\,\mathrm{fb}^{-1}$ for the tW channel.

W+jets

The final state is achieved when a W boson, decaying into a muon and a neutrino, is produced in association with jets.

The NNLO cross section for the production of leptonically decaying W bosons is approximately 37 509 pb. This is calculated with the FEWZ (Fully Exclusive W and Z Production) simulation code [59]. In fact, W+jets processes are generated as a function of the jet multiplicity. This analysis will only use the W+3 jets and the W+4 jets samples as no events from lower jet multiplicity samples pass the selection criteria in the next section.

The integrated luminosity of the W+jets sample is approximately 50 fb^{-1}.

Z+jets

A Z boson is produced in association with jets and decays into a muon pair, of which the second muon is not observed or does not pass the selection criteria.

The NNLO cross section for leptonically decaying Z bosons is approximately 3 503.71 pb [60]. The cross section was calculated with the same package as that of the W+jets sample and the same remarks apply.

The integrated luminosity of the Z+jets sample is approximately 225 fb^{-1}.

QCD multi-jet events

As leptons can be produced within jets, the desired final state can be obtained. In general, these leptons are not isolated and have a low p_{T}, but, as the cross section of these processes is large, contributions from multi-jet events cannot be ruled out completely.

As is discussed in the following section, the selection criteria rule out most of the multi-jet events. Therefore, this background will not be simulated.

5.3 Selection Requirements

Only events that pass the trigger requiring an isolated muon with a p_{T} larger than 24 GeV and a pseudo-rapidity $|\eta| < 2.1$ are used. The efficiency of the trigger is not the same for the data and the simulation. Therefore, a scale factor is implemented for the simulated samples. As the trigger efficiency depends on the p_{T} and η of the muon, also the scale factors depend on these variables. The scale factors are defined as the ratio of the trigger efficiency in data and the trigger efficiency in simulated $\mathrm{Z} \rightarrow \mu\mu$ events. [61]

Then, a good primary vertex is sought. As the LHC collides bunches of protons, each containing billions of particles, it is possible that more than one proton pair collides during the same bunch crossing. This results in several primary vertex candidates. The correct one is determined with the aid of the impact parameter. In the z direction the impact parameter must be smaller than 24 cm and it must be smaller than 2 cm in the transverse plane. If there is more than one PV that fills these requirements, the one maximising the sum of the p_{T}^2 of its tracks is chosen. The amount of pile-up energy of the so-called underlying event is related to the number of primary vertices. The average number of primary vertices per event is visualised in Figure 5.2(a). The number of PVs in the simulation does not correspond with the number of PVs in the data. Therefore, a scale factor is applied to the simulation. The resulting distribution is shown in Figure 5.2(b).

To get the final state defined in Section 5.1, exactly one isolated muon is required. This must have a p_{T} larger than 25 GeV and a pseudo-rapidity $\eta < 2.1$. On top of that, events containing a second muon with a p_{T} larger than 10 GeV or

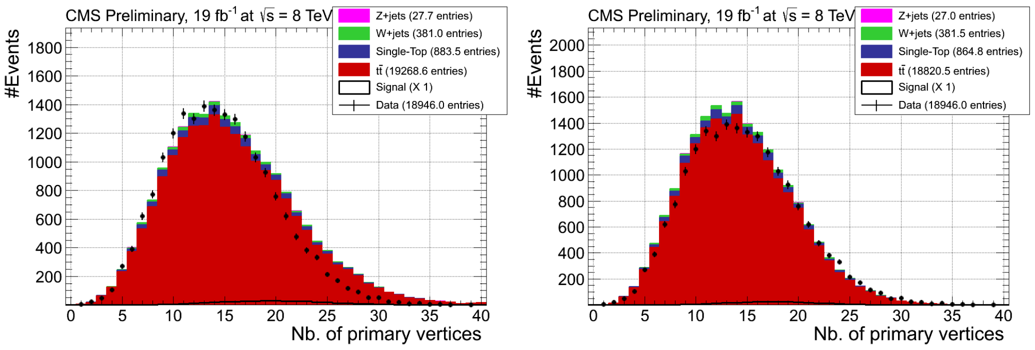

(a) (b)

Figure 5.2: Number of primary vertices before (a) and after (b) the application of a scale factor for pile-up in the simulation. The last bin contains the overflow.

an electron with a $p_{\mathrm{T}} > 30\,\mathrm{GeV}$ are rejected if these are better isolated than relIso 0.2, resp. 0.15.

Further, the event is required to have at least four jets. Four of these are produced by the stop quark pair, but additional jets can result from pile-up, the fragments of the protons and gluon radiation. To avoid selecting events with many of these low-energetic jets, a p_{T} threshold of 30 GeV is imposed. At least two jets need to be identified as b jets to produce the desired final state. This is done with the CSV algorithm using the medium working point. As mentioned in Section 4.3, D hadrons can also produce a secondary vertex, which opens the possibility that a c jet is mistakenly identified as a b jet. Also light jets can be identified as b jets (mistagging), although to a lesser extent. Scale factors are applied to take the different mistag rate in data and simulation into account, as explained in Appendix B. Figure 5.3 shows the number of selected jets and the number of b-tagged jets per event after requiring one isolated muon and four jets. Most events have four jets, but a non-negligible amount of events has five up to eight jets. The decrease in the number of jets is less pronounced for the $\mathrm{t\bar{t}}$ sample than for the other background samples. Figure 5.3(b) shows that most events have no jets that were identified as b jets, but the downward trend is not reflected in each sample. The amount of $\mathrm{t\bar{t}}$ and ST events even increases when one b-tagged jet is found. Requiring at least two b jets is thus very effective to discriminate against some background processes, in this case the W+jets and the Z+jets sample. This can also be demonstrated by explicitly using the discriminating value of the b-tag algorithm. Figure 5.4(a) shows the b-tag value of the hardest jet. Using the medium working point of the CSV algorithm, b jets are only identified as such when the b-tag value is higher than 0.679. It is clear that the majority of W+jets and Z+jets events will not be selected. Figure 5.4(b) shows the b-tag value of the jet with the highest b-tag value. Whereas the $\mathrm{t\bar{t}}$ distribution peaks at high b-tag values, this is not the case for W+jets and Z+jets.

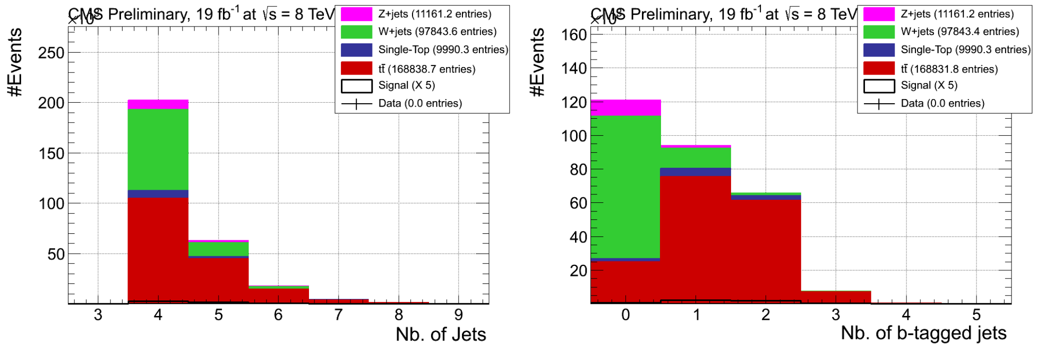

(a) (b)

Figure 5.3: Number of selected jets per event (a) and number of b-tagged jets per event (b) after requiring exactly one isolated muon and at least four jets.

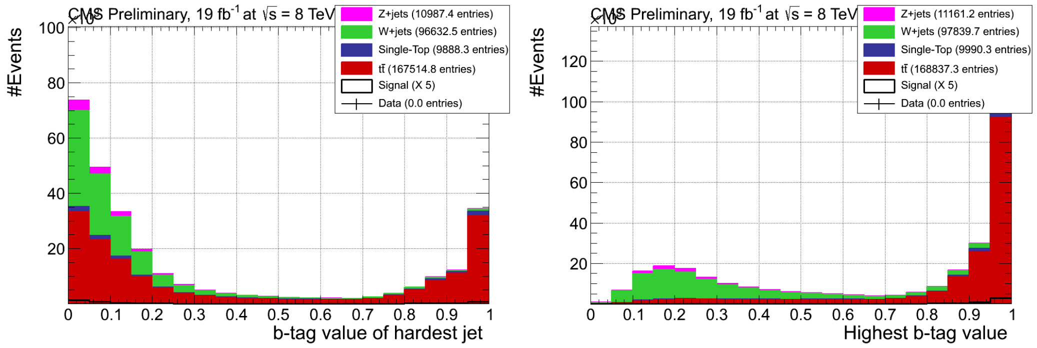

(a) (b)

Figure 5.4: (a) b-tag value of the hardest jet; (b) highest b-tag value in the event. Only events with exactly one isolated muon and at least four jets are considered.

In addition to the selection criteria above, which select the correct final state, cuts are imposed on variables that increase the signal to background ratio. Only events where the missing transverse energy $\not{E}_{\mathrm{T}}$ (or MET) is larger than 70 GeV and the scalar sum of the transverse momenta of the four jets with the highest p_{T}, $H_{\mathrm{T}} = \sum_{i=1}^{4} p_{\mathrm{T,i}}$, is at least 250 GeV are selected.

A summary of these selection requirements can be found in Table 5.1. The signal enhancing effect of the H_{T} and $\not{E}_{\mathrm{T}}$ cuts is clearly visible. About 30% of the signal events are rejected, but the amount of rejected background events increases to about 70% for the $\mathrm{t\bar{t}}$ and even 90% for the Z+jets sample. This is also clear from Figure 5.5, where the distributions of $\not{E}_{\mathrm{T}}$ and H_{T} are shown before their respective cuts. The overshoot of data events in Figure 5.5(a) is due to QCD multi-jet events. The large $\not{E}_{\mathrm{T}}$ cut rules out most of these events and, combined with a cut on H_{T}, such a large portion of the multi-jets is rejected, that it will not be necessary to simulate this background process. As a result, multi-jet processes will not be considered in the remainder of this analysis.

Table 5.1: Summary of the selection cuts and their effect on the total number of events in the different datasets.

	Data	*Signal*	$t\bar{t} + jets$	$st + jets$	$W + jets$	$Z + jets$
trigged & good PV	2.24097e+06	2056.67	452792	52950.6	925233	160370
1 selected muon	1.79582e+06	1746.01	371663	43757.6	777920	96274.1
Veto 2nd muon	1.71507e+06	1743.81	364421	43475.8	777864	61617.9
Veto electron	1.6922e+06	1739.32	346611	42636.7	776087	61123.6
$\geq$ 4 jets	319963	1000.27	168827	9990.24	97833.9	11161.1
$\not{E}_{\mathrm{T}} > 70$ GeV	96142	818.58	62559.6	3689.31	29202.8	1327.55
$H_{\mathrm{T}} > 250$ GeV	71462	689.352	47465.8	2786.46	22138.2	1038.5
$\geq$ 2 b-jets (CSVM)	18946	276.63	18820.5	864.788	381.496	26.9675

Including the signal, the total number of simulated events is equal to 20 370, compared to only 18 946 events in the data sample. The undershoot of data can be explained by the systematic uncertainty on the integrated luminosity, which is about 4.4%, and the systematic uncertainties on the production cross sections of the background processes.

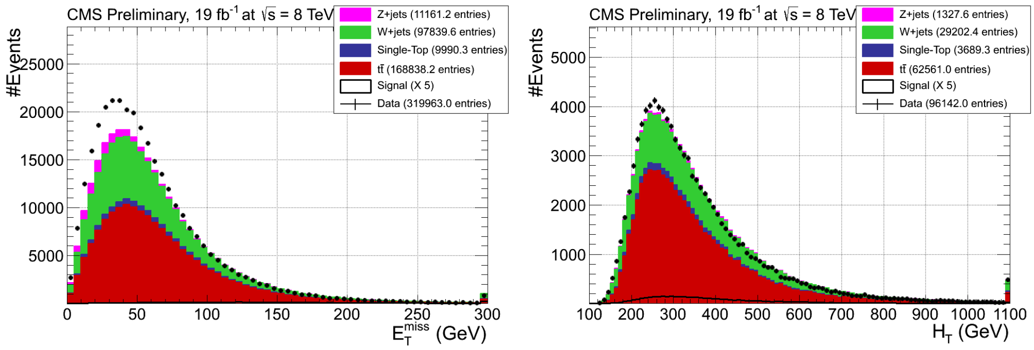

(a) $\not\!\!E_T$ (b) H_T

Figure 5.5: Distributions of the $\not\!\!E_T$ (a) and H_T (b) before their respective cuts. The last bin contains the overflow.

6

Event Reconstruction

A particle detector only registers the final state of the event. In case of the event topology in Section 5.1 there are four jets, one muon and missing transverse energy. These objects can be recombined to W bosons, top and stop quarks. This is not trivial since it is not clear which jet originated from which parton. Therefore, simulated samples are used to determine the expected distribution of the reconstructed mass of the W boson and the top quark by matching the jets to the partons and recombining them into the correct objects. For each possible combination in the reconstructed event, a kinematic variable reflecting the agreement with the expected W boson and top quark masses is calculated. This way, the simulated samples and the data sample are treated on the same level, without explicitly using the parton information.

6.1 Jet-Parton Matching

The jet-parton matching is carried out using the simulated $\mathrm{t\bar{t}}$ sample. This sample also contains generated events, where each particle is associated with an identifying number or pdgID [3]. This enables to reconstruct the decay chain, as not only the pdgID of the particle itself, but also that of its 'mother' and 'grandmother' particle can be retrieved. Only those simulated events where the full expected decay chain of the top quark is recovered from the kinematics of the observed objects are used. The expected distribution of the W boson and top quark masses is obtained from these events.

The jets will be matched with the quarks using an algorithm that orders the quarks according to descending p_T values and minimises the sum of the distances between the four quarks and the jets. These distances are defined as,

$$\Delta R = \sqrt{(\eta_\mathrm{jet} - \eta_\mathrm{quark})^2 + (\phi_\mathrm{jet} - \phi_\mathrm{quark})^2}\,, \tag{6.1}$$

and cannot exceed 0.3 for each jet–quark pair.

Using the pdgIDs of the quarks, the masses of the reconstructed hadronically decaying W boson and the corresponding top quark are calculated. The mass distributions are shown in Figure 6.1 and fitted with a Gaussian function in an interval defined by the root-mean-square (RMS) around the bin containing the maximum number of events. The fitted W mass is 85.9 ± 10.0 GeV and the top mass is 179 ± 15 GeV.

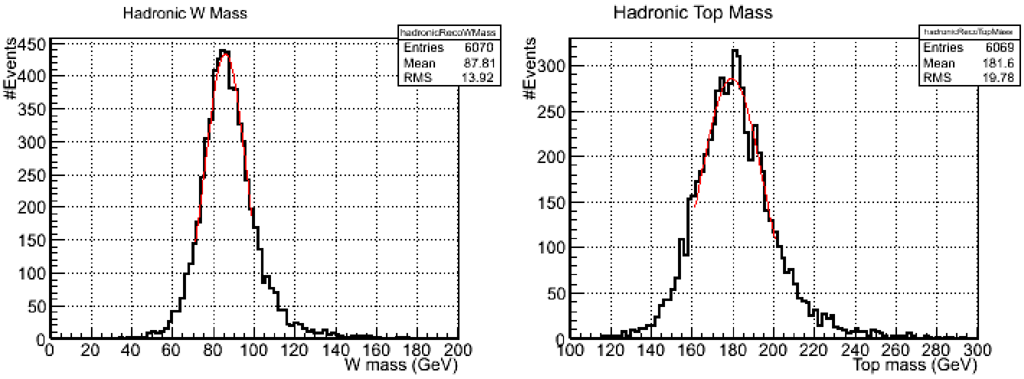

(a) (b)

Figure 6.1: Reconstruction of the W boson mass (a) and the top quark mass (b), using $t\bar{t}$ events for which the jets are matched to the quarks at generator level.

6.2 Jet-Parton Association

When there is no information about the identity of the particle that created the jet, which is the case for the collision data, other methods must be applied. If the event is a true semi-muonic $t\bar{t}$ event, the combination of two light jets should give rise to a reconstructed particle with a mass resembling that of the W boson and the combination of this reconstructed particle with a b jet should give a top quark.

If there are only four jets present in the event and the b jets are b tagged, the light jets are easily identified. There are still two possibilities for the b jets, one coming from the hadronically decaying top quark and the other from the leptonically decaying one. A χ^2 method is applied to see which jet combination best reflects the kinematics in the top quark decay, more specifically the masses of the W boson and the top quark,

$$\chi^2 = \left(\frac{m_{\mathrm{j1,j2}} - m_{\mathrm{W}}}{\delta m_{\mathrm{W}}} \right)^2 + \left(\frac{m_{\mathrm{j1,j2,j3}} - m_{\mathrm{t}}}{\delta m_{\mathrm{t}}} \right)^2 , \tag{6.2}$$

where $m_{\mathrm{j1,j2}}$ is the mass of a reconstructed particle formed by two light jets and $m_{\mathrm{j1,j2,j3}}$ is the mass of the combination of the previously mentioned light jets and a b jet. m_{W} (m_{t}) is the mass of the W boson (top quark) and δm_{W} (δm_{t}) the square-root of the variance obtained from the fit, as explained in Section 6.1.

If there are more than four jets in the event, only the four with the highest transverse momentum are considered. Sometimes this subset will only contain one b-tagged jet. When this is the case, the other b-tagged jet is taken from the remainder of the jet collection.

Figure 6.2 shows the reconstructed W boson and top quark mass for the jet combination with the smallest χ^2. The distribution of the mass of the W boson is centred around 85 GeV and that of the top quark is centred around 180 GeV. These values correspond to the reconstructed masses obtained in Section 6.1, as is to be expected.

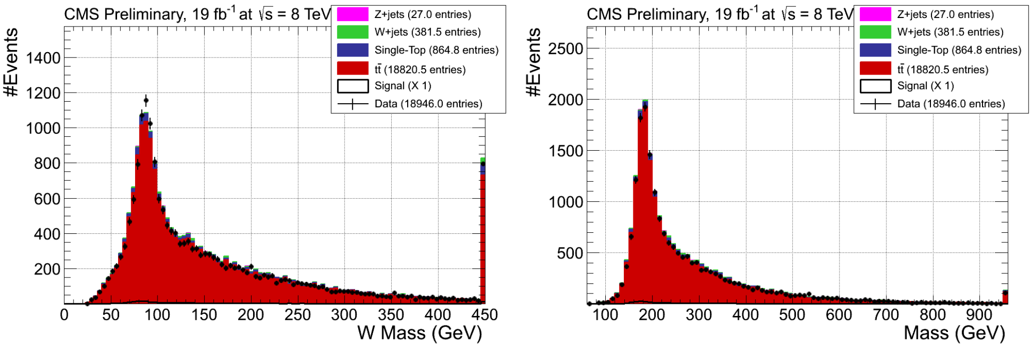

(a)

(b)

Figure 6.2: Reconstructed W boson mass (a) and top quark mass (b) for the jet-quark assignment chosen with a χ^2 method. The last bin contains the overflow.

To determine the efficiency of the χ^2 method, the chosen jet-quark assignment is compared with the best jet-quark assignment for the events in which the true jet-quark assignment is reconstructed. The chosen jet-quark assignment is correct for about 74% of these matched events. If a random jet-quark assignment is chosen, the correct assignment would be achieved in only one out of 12 cases[1] or about 8.3%. This proves that the χ^2 method, together with b-tagging, is very effective.

---

[1] Four jets give rise to 24 possible jet combinations, but the order of the W jets does not matter for the reconstruction of the W boson mass.

7

The Matrix Element Method

The Matrix element method (MEM) is a fairly recent technique that was first introduced at the TEVATRON collider to make a more precise measurement of the top quark mass [62,63]. It will be shown to be also useful for analyses where a small signal has to be extracted from a large background. Traditionally, these analyses make use of multivariate analysis techniques like neural networks, where several variables that are sensitive to the signal are combined in order to make a variable that is even more sensitive. As the matrix element method uses all information contained in the event, it is expected that this method is more sensitive than MVA techniques, which use only a subset of information.

This chapter will describe the matrix element method and explain how it is used in this analysis. Chapter 8 will compare this technique's sensitivity to stop quark production with that of a standard kinematic observable, in this case $H_\mathrm{T} + \not{E}_\mathrm{T}$.

7.1 The Matrix Element Method in a Nutshell

The MEM uses the theoretical matrix element to calculate the probability that a certain process is produced and observed assuming a specific theoretical model [64]. The observed event is characterised by a set of measured four-momenta p^{obs} and the probability density is defined as,

$$\mathcal{P}\left(p^{obs}\middle|\vec{\theta}\right) = \frac{1}{\sigma(\vec{\theta})}\int dp^{true}\,\left|\mathcal{M}\left(\vec{\theta}\middle|p^{true}\right)\right|^2 R\left(p^{true}\middle|p^{obs}\right)\,, \tag{7.1}$$

where $\vec{\theta} = \theta_1, ..., \theta_n$ are the parameters of the physics model, $\mathcal{M}(\vec{\theta}|p^{true})$ is the theoretical matrix element of the specific process, $\sigma(\vec{\theta})$ is the total cross section of the process and $R(p^{true}|p^{obs})$ is the transfer function.

The matrix element will be calculated at leading order using the parton four-momenta. The four-momenta of the objects are parametrised as E, θ and ϕ. As the partons hadronise and the detector has a limited resolution, this does not correspond to the momenta that are actually observed. Also interactions with the detector material, like multiple scattering, will contribute to the difference between the observed and theoretical momentum of a particle. In order to take these detector effects into account, the matrix element will be convolved with a detector response or transfer function.

$$\left|\mathcal{M}\left(\vec{\theta}\middle|p^{true}\right)\right|^2 \longrightarrow \int dp^{true} \left|\mathcal{M}\left(\vec{\theta}\middle|p^{true}\right)\right|^2 R\left(p^{true}\middle|p^{obs}\right) . \tag{7.2}$$

The transfer function will map the observed momenta to the ‘true’ momenta and vice versa.

In this analysis, only the transfer functions of the jet energies were calculated, separately for b jets and non-b jets. For the jet angles, θ and ϕ, and for the muon momenta δ functions are applied. This is equivalent to assuming that these quantities are perfectly measured. Since transfer functions relate the observed momenta to the true momenta, only reconstructed objects that are matched with the true objects in the simulation are used. The $\mathrm{t\bar{t}}$ events that are matched according to the description in Section 6.1 fulfil these requirements.

For b jets, the difference between the parton and the jet energy, ΔE, can be found in Figure 7.1. The difference is plotted as a function of four parton energy bins (Fig. 7.1(a)). For all these bins, the mean value of the energy difference is close to zero. The width of the distribution, however, is not negligible. This is visualised in Figure 7.1(b), where the number of entries in the second parton energy bin is plotted as a function of the energy difference.

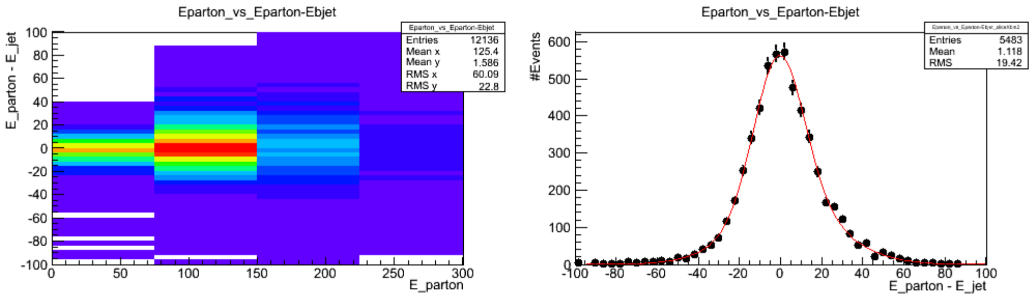

(a) (b)

Figure 7.1: (a) Difference between the parton and jet energy as a function of the parton energy; (b) Close-up of $75\,\mathrm{GeV} < E_{\mathrm{parton}} < 150\,\mathrm{GeV}$, showing the number of entries as a function of the difference between the parton energy and the jet energy. Each bin is fitted with a double Gaussian.

As the tails are quite large, each parton energy bin is fitted with a double Gaussian,

$$f(\Delta E) = \frac{1}{a_3}\exp\left[-\frac{1}{2}\left(\frac{\Delta E - a_1}{a_2}\right)^2\right] + \frac{1}{a_6}\exp\left[-\frac{1}{2}\left(\frac{\Delta E - a_4}{a_5}\right)^2\right] , \tag{7.3}$$

where $a_1, ..., a_6$ are free parameters. These are fitted as a function of the parton energy, using

$$a_i(E) = a_{i,0} + a_{i,1}\sqrt{E} + a_{i,2}\,E\,, \tag{7.4}$$

where $a_{i,0}, a_{i,1}, a_{i,2}$ are the coefficients of the evolution of the parameter a_i. So each transfer function has a total of 18 parameters, of which the values can be found in Table 7.1 for the b-jet energy. The narrow Gaussian, defined by parameters a_4 to a_6, fits the peak of the distribution and its expectation value is compatible with zero. The broad Gaussian, described by a_1 to a_3, fits the tails of the distribution.

Table 7.1: Parameters of the transfer function for the b-jet energy.

	a_{i0}	a_{i1} ($\sqrt{E}$)	a_{i2} (E)
a_1	a_{10} = -41.73±25.32	a_{11} = 8.14±5.73	a_{12} = -0.38±0.29
a_2	a_{20} = 35.51±122.49	a_{21} = -4.97±28.83	a_{22} = 0.30±1.46
a_3	a_{30} = -316.39±408.81	a_{31} = 86.44±91.99	a_{32} = -4.04±4.13
a_4	a_{40} = -3.52±5.30	a_{41} = 0.65±1.11	a_{42} = -0.04±0.06
a_5	a_{50} = 6.89±55.40	a_{51} = -0.49±12.81	a_{52} = 0.10±0.64
a_6	a_{60} = 21.55±10.37	a_{61} = -3.23±1.98	a_{62} = 0.12±0.09

Since the transfer function has a certain width, each observed jet energy has a certain probability to come from a quark with a specific true energy. Therefore, an integration over these true momenta is carried out. A normalisation factor is included in the transfer function to be able to interpret Equation (7.1) as a likelihood.

7.2 Implementation in MadWeight

The integral in Equation (7.1) will be calculated with `MadWeight` [65,66]. This is a `MadGraph` based tool. The input file, containing the kinematic information of the events, is the so-called LHCO file [67] and needs to be written in a special format. An example of a $t\bar{t}$ event can be found below.

```
#    typ      eta      phi       pt      jmas     ntrk    btag
0             1         0
1    4    0.8864    0.3375    114.6885    20.745    0.00    1.000
2    4    0.5797    -0.3712    52.3088    10.452    0.00    0.000
3    4    1.7213    3.0647    50.5418    9.595    0.00    0.000
4    4    -0.9624    2.3365    72.8960    12.887    0.00    1.000
5    2    -0.8966    0.3250    32.7285    0.106    -1.000    0.000
6    6    0.0000    -1.0883    72.5485    0.000    0.00    0.000
```

The first line is commented and indicates the content of each column. Each new event start with a row labelled with “0”, followed by the event and/or run number. Each following row is related to an observed object in the event. The second column indicates the type of the particle. `4` corresponds to a jet, `2` to a muon and `6` to a neutrino. The next columns contain the pseudo-rapidity η, the azimutal angle ϕ, the transverse momentum p_{T} and the mass of the particles. The `ntrk` column is used to indicate the charge of the lepton. The column labelled with `btag` allows for the possibility to label jets as b jets (`1.000`) or otherwise (`0.000`).

Some conditions apply to the values of the variables that are written in the file. If these are not taken into account, `MadWeight` will return an error.

- `MadWeight` does not recognise a negative zero value. So if η would be equal to -0, it needs to be replaced by `0.0`.
- As $-\pi$ and $+\pi$ describe the same point on the circle, only $+\pi$ is included in the allowed-values interval.
- All masses smaller than 0.001 GeV are replaced by zero. This avoids writing down extremely small, but not quite zero masses.

Also the order of the particles is important. It needs to be consistent with the order of the particles in the generation of the process. The above example was generated as follows,

```
generate p p > t t~ , ( t > b w+ , w+ > q q ) , (t~ > b~ w- , w- > mu- vm~ )
    @1
```

where the tilde indicates an antiparticle. The first three particles in the list thus originate from the top quark and the last three particles originate from the anti-top quark. Particles one and four are b jets. As this order is strictly adhered to, `MadWeight` has an option to automatically permute the jets. It will then calculate the average of the integral values obtained by all possible jet combinations. The drawback is that the integration time strongly depends on the number of jet combinations, which is 24 in the case of $\mathrm{t\bar{t}}$ events.

A jet-quark assignment was already chosen using the χ^2 method explained in Section 6.2. Therefore, the integral needs to be calculated for only two jet combinations. To avoid that the integral is computed for more jet combinations, each event is added twice to the LHCO file, manually switching the order of the jets from the W boson. Afterwards, the values of the two calculations are averaged.

Another aspect that has a large impact on the integration time is the number of integration points. The standard value is 50 000. To investigate the effect of decreasing this amount, an integration with 100 000 integration points was carried out to get a very precise measurement of the integral. Then, the same events were used for an integration with 10 000, 20 000, 30 000, 40 000 and 50 000 integration points. Compared to the measurement with 100 000 integration points, the one with 50 000 had a relative uncertainty that was almost twice as large. On the other hand, the measurement with 30 000 integration points was only slightly worse than the one with 50 000, but was about 40% faster. For 10 000 integration points the relative uncertainty increased rapidly, while generating only a moderate time gain. Balancing speed and accuracy, 30 000 integration points are chosen.

Also the transfer functions have an impact on the integration time. This is why only the transfer functions for the jet energies (both b and non-b) were implemented.

With these settings, the average integration time for a $\mathrm{t\bar{t}}$ event, with two jet combinations, is about 15 min. In the meantime, developments in `MadWeight` continued and, recently, the integration time is reduced by a factor ten or more.

8

Sensitivity of the Matrix Element Method for Stop Quark Searches

8.1 Calculation of the Probability Density for Different Hypotheses

The matrix element method returns the probability that a certain observed event is consistent with a specific physics hypothesis. The underlying hypothesis or physics process can be a stop quark pair process (signal), but also a background process. Therefore, the probability is calculated for both the signal and the background hypothesis. The latter is represented by $\mathrm{t\bar{t}}$ production, which is by far the dominant background. This means that there are four integral calculations per event, as there are two possible jet combinations and two hypotheses.

The integrals are calculated with `MadWeight`, as is explained in Section 7.2, and the values obtained from the different jet combinations are averaged. Also a weighted average, where higher integral values got a higher weight, was investigated, but this turned out to have little effect.

The normalisation factor is defined by the cross section of the process. As an event selection reduces the number of events, the cross section needs to be multiplied by the selection efficiency, which is about 2.37% for the $\mathrm{t\bar{t}}$ sample and about 10.69% for the signal. Combined with the cross-section times branching ratio mentioned in Section 5.1, the normalisation factors become 51.7 for the signal and 1.26 for the $\mathrm{t\bar{t}}$ sample.

With these components, the probability in Equation (7.1) can be computed. Some approximations were made in the calculations of the normalisation factor and the transfer functions, and it was not verified if $\mathcal{P}(p^{obs}|\vec{\theta})$ can truly be interpreted as a probability. A probabilistic interpretation of $\mathcal{P}(p^{obs}|\vec{\theta})$ is not necessary for this analysis, since the probabilities are merely used to construct a variable to discriminate between two physics hypotheses.

Figure 8.1 shows the probabilities for events coming from the simulated signal, $\mathrm{t\bar{t}}$ and W/Z+jets samples, where the last two are combined under ‘other’. $\mathcal{P}(p^{obs}|\tilde{\mathrm{t}}\bar{\tilde{\mathrm{t}}})$ is indicated by $\mathrm{P}(S)$ and $\mathcal{P}(p^{obs}|\mathrm{t\bar{t}})$ by $\mathrm{P}(B)$. As the probabilities are very small, the negative logarithm of the probabilities is displayed. This means that the highest values of the probabilities can be found in the bottom left corner.

Figure 8.1(a) shows the probabilities for the signal sample. These seem to be ordered on a bisector with a tail in the x direction. For low x values, i.e. high probabilities when a signal hypothesis is assumed, the spread in the y direction is much larger than that in the x direction. This means that the events resemble the signal hypothesis more than the background hypothesis.

The probabilities for the $\mathrm{t\bar{t}}$ sample can be found in Figure 8.1(b). Figure 8.1(c) shows the probabilities for $\mathrm{t\bar{t}}$ events where the jets were matched to the partons at generator level. A comparison of both plots shows that the tail of the distribution and most of the width of the bisector arise from incorrect jet-quark assignments.

Figure 8.1(d) shows the probabilities for W+jets and Z+jets events. These are expected to resemble the signal and the background hypothesis equally well. This is indicated by a rather narrow bisector.

8.2 Sensitivity of Different Observables

8.2.1 Likelihood ratio

The probabilities in Section 8.1 are used to make a discriminating variable. This analysis will use the likelihood ratio (LR), which is defined as

$$LR = \frac{\mathrm{P}(S)}{\mathrm{P}(S) + \mathrm{P}(B)} \,. \tag{8.1}$$

The distribution of this variable is plotted in Figure 8.2, using both a linear scale (a) and a logarithmic scale (b). Most events are found in the first and last bin. The first bin is expected to contain events that bear resemblance to background events and the last bin to contain events that look like signal events.

To determine the sensitivity of the likelihood ratio, the signal-to-background ratio $S/\sqrt{B}$ is determined. All events with a LR value below a certain cut value are removed and $S/\sqrt{B}$ is calculated from the remaining events. The result is shown in Figure 8.3. The binning is ten times finer than in Figure 8.2 to get a good view of the tiniest changes.

As is expected, it is better to either apply no cut on the likelihood ratio or to apply a cut close to one. The steep increase at the last bin, however, suggests that, even with this fine binning, most of the sensitivity is contained in the last bin. The significance also gives an indication of the sensitivity that would be achieved if the likelihood ratio was used in a simple cut-and-count technique.

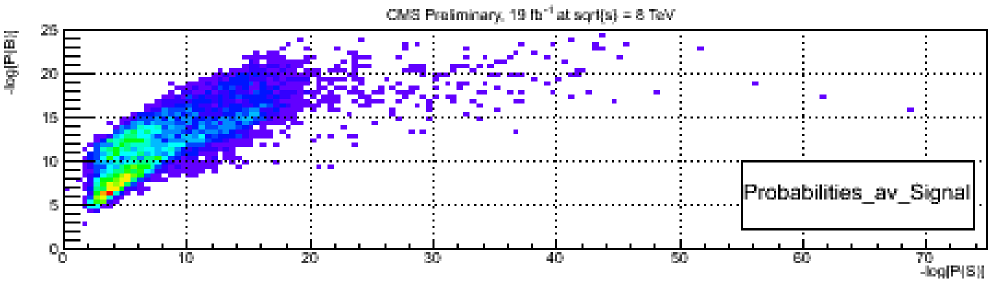

(a) Signal

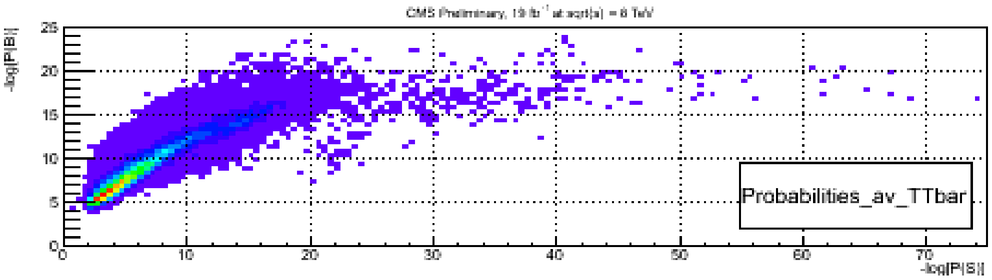

(b) $t\bar{t}$

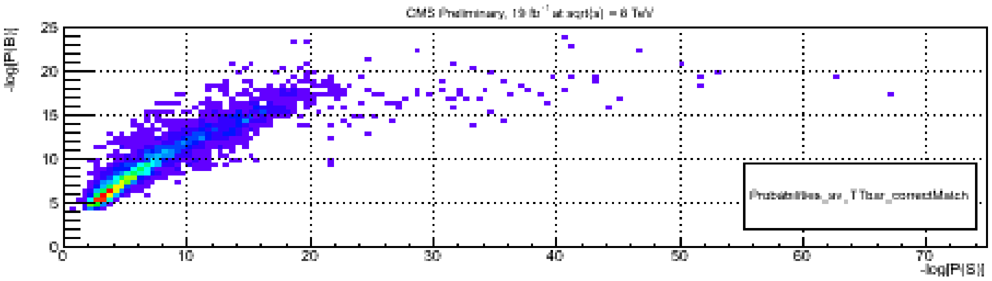

(c) Matched $t\bar{t}$

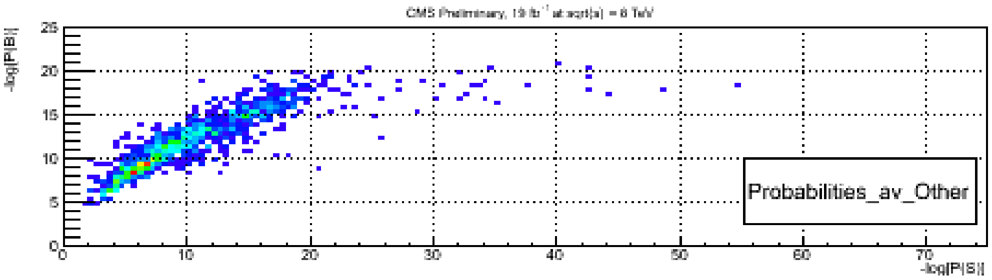

(d) W+jets and Z+jets

Figure 8.1: Two-dimensional histograms of the negative logarithm of the probabilities for different simulated samples, using a signal hypothesis (x axis) and background hypothesis (y axis).

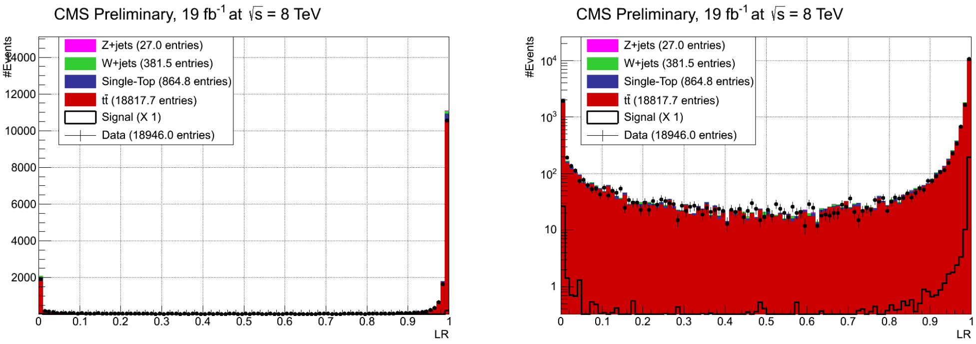

(a) Linear scale (b) Log scale

Figure 8.2: Likelihood ratio distribution obtained with the matrix element method.

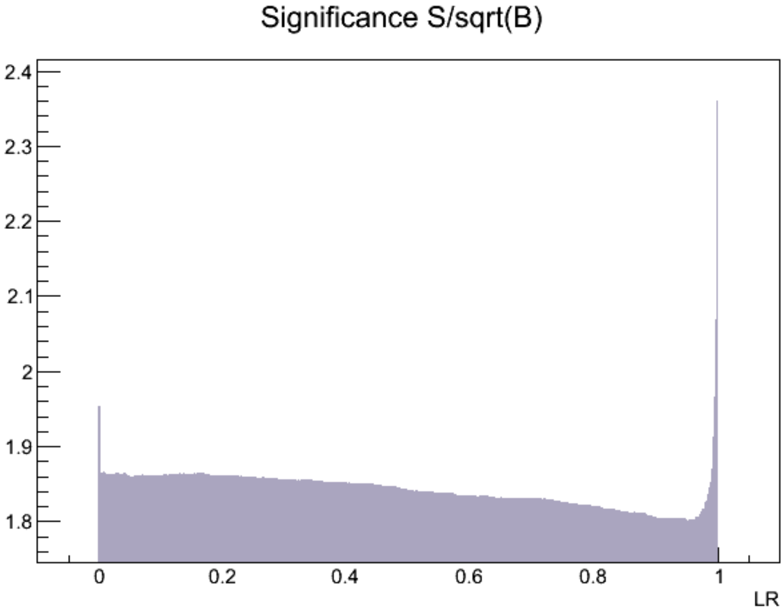

Figure 8.3: Significance $S/\sqrt{B}$ of the likelihood ratio.

8.2.2 Regular kinematic observable

The event topology in Section 5.1 showed that the main differences between signal and background processes are the amount of missing transverse energy and the transverse momentum of the particles. A variable combining these two features should thus have a certain sensitivity to the signal. A simple observable is $H_T + \not{E}_T$ and its distribution is plotted in Figure 8.4.

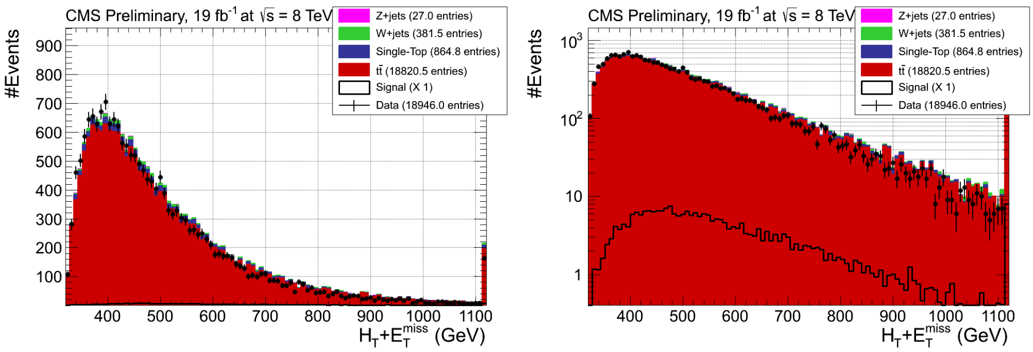

(a) Linear scale

(b) Log scale

Figure 8.4: $H_\mathrm{T} + \not{E}_\mathrm{T}$ distribution. The last bin contains the overflow.

Figure 8.5 shows the normalised distribution of $H_\mathrm{T} + \not{E}_\mathrm{T}$ for the signal and the $\mathrm{t\bar{t}}$ sample. The signal is shifted to slightly higher values of $H_\mathrm{T} + \not{E}_\mathrm{T}$.

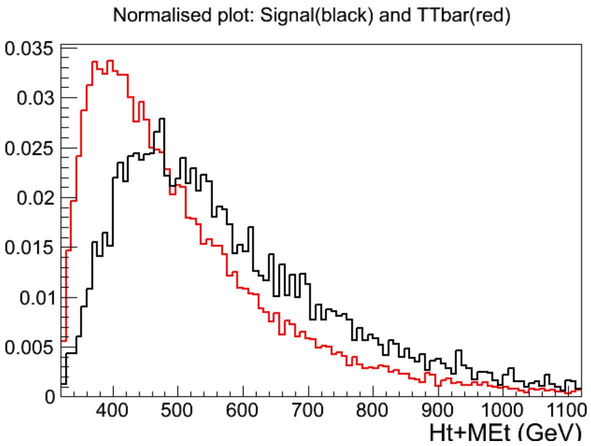

Figure 8.5: Normalised distribution of the signal (black) and $\mathrm{t\bar{t}}$ (red) sample.

The significance of the distribution is displayed in Figure 8.6. The sensitivity is the highest at about 400–450 GeV and a harder cut results in a reduced sensitivity.

8.2.3 Transformation of the likelihood ratio

Compared to the likelihood ratio distribution, $H_\mathrm{T} + \not{E}_\mathrm{T}$ is sensitive over its entire range. This begs the question if the sensitivity of the likelihood ratio can be increased by spreading the sensitive information contained in the last bin. This is done with a logarithmic function,

$$-\log\left[(1 - LR) + 10^{-5}\right] . \tag{8.2}$$

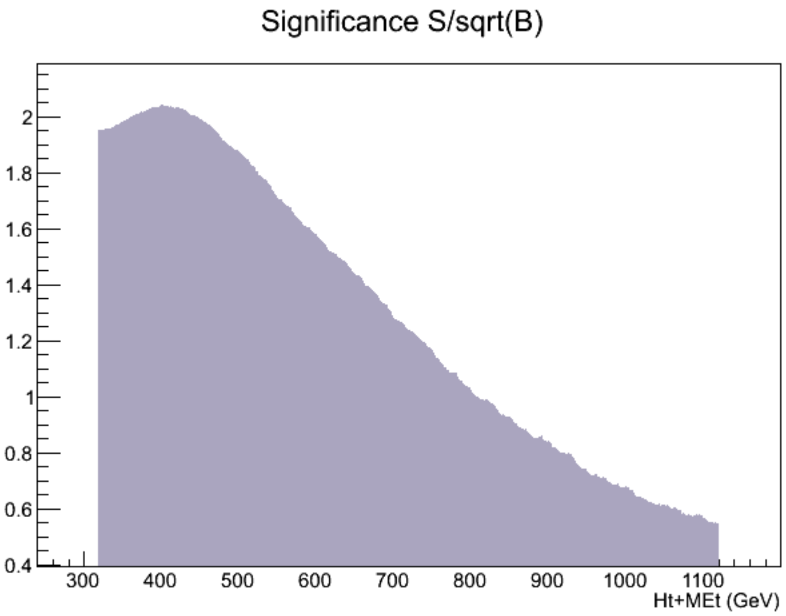

Figure 8.6: Significance $S/\sqrt{B}$ of the $H_\mathrm{T} + \not{E}_\mathrm{T}$ distribution.

As a logarithm diverges when it approaches zero, a term 10^{-5} is added to ensure a finite range. Otherwise, the majority of the events would end up in an overflow bin, rendering the transformation quite useless. The minus sign simplifies the comparison with the ordinary likelihood ratio, as the left-hand side of Figure 8.2 remains on the left in Figure 8.7, which contains the distribution of this transformed variable.

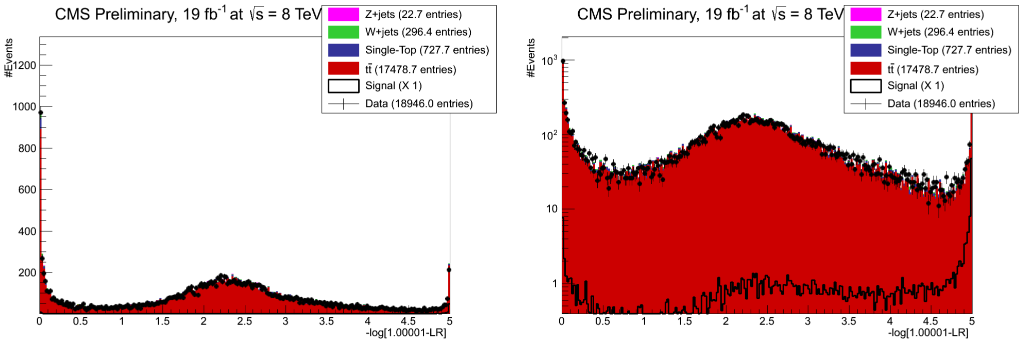

(a) Linear scale

(b) Log scale

Figure 8.7: Transformed likelihood ratio distribution, $-\log\left[(1 - LR) + 10^{-5}\right]$.

Figure 8.8 shows the significance for the transformed likelihood ratio. The difference with Figure 8.3 is immense. The sharp peak is replaced by a gradual increase and the top significance rises from about 2.4 to approximately 3.3.

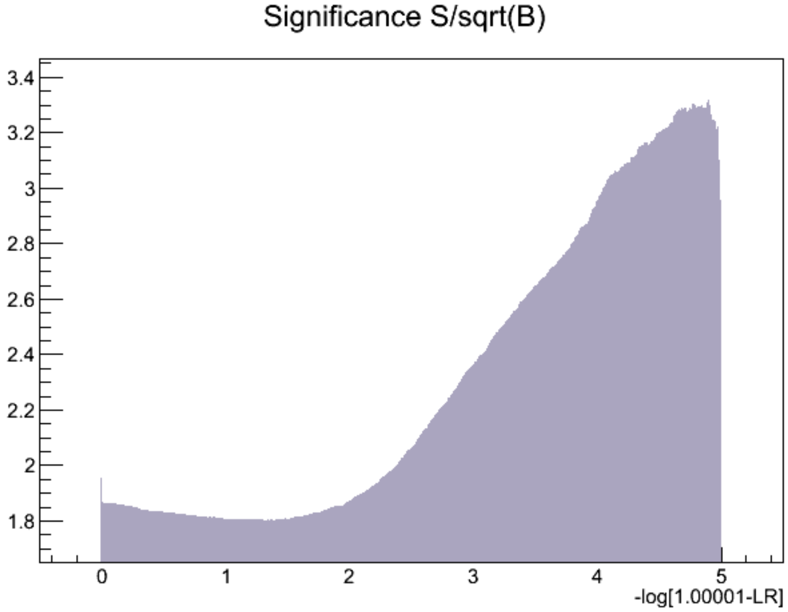

Figure 8.8: Significance $S/\sqrt{B}$ of the transformed likelihood ratio distribution.

8.3 Upper Limit on the Signal Cross Section

The shape of Figures 8.3, 8.6 and 8.8 indicates that the transformed likelihood would give the best result if a cut-and-count method was applied. To be able to exclude the mass point (or claim discovery) more information is necessary and a statistical analysis is performed. Template or shape fitting is preferred over a cut-and-count method, since it is more sensitive.

Two hypotheses are postulated, one where all the events are background events and one where the events are a mixture of signal and background. Since the data are binned, the likelihood of these hypotheses can be described with a Poisson distribution,

$$\mathcal{L}(\text{data}|\mu) = \prod_i \frac{(\mu s_i + b_i)^{n_i}}{n_i!} \, e^{-(\mu s_i + b_i)} \,, \tag{8.3}$$

where μ is the signal strength and n_i the observed number of events in bin i and s_i (b_i) are the predicted number of signal (background) events in bin i. For the background-only hypothesis, the signal strength is equal to zero.

The compatibility of the data with the background or the signal-plus-background hypothesis is determined by a test statistic,

$$t_\mu = -2 \ln \lambda(\mu) \,, \qquad \text{with } \lambda(\mu) = \frac{\mathcal{L}(\text{data}|\mu)}{\mathcal{L}(\text{data}|\hat{\mu})} \,, \tag{8.4}$$

where $\lambda(\mu)$ is the profile likelihood ratio (PLR) and $\hat{\mu}$ is the best fit value of the signal strength. As the rate of signal events cannot be negative, $\hat{\mu}$ must be ≥ 0. To avoid that upward fluctuations of the data would contribute in rejecting the signal hypothesis, $\hat{\mu}$ is also constrained to be $\leq \mu$.

The PLR takes values between zero and one, where one indicates a good agreement between the best fit obtained from the data, and the hypothetical signal strength. As a consequence, high values of t_μ favour a background-only hypothesis. The level of disagreement between a measurement and the hypothesis can be quantified by a p-value, which indicates the fraction of future measurements that would give a worse result. This value is defined by

$$p_{s+b} = \int_0^{t_\mu^{\text{obs}}} f(t_\mu|\mu)\, dt_\mu \,, \tag{8.5}$$

for the signal-plus-background hypothesis and

$$p_b = \int_{t_\mu^{\text{obs}}}^{\infty} f(t_\mu|0)\, dt_\mu \,, \tag{8.6}$$

for the background-only hypothesis, where $f(t_\mu|\mu)$ is the probability density function of t_μ assuming a signal strength μ. The probability density functions are constructed using simulated pseudo-data or ‘toys’ [68]. In general, the distributions resemble χ^2 functions and, when each bin contains enough events, these can be approximated by asymptotic formulas [69].

Systematic uncertainties can be taken into account by introducing nuisance parameters, indicated by α. The PLR then becomes

$$\lambda(\mu) = \frac{\mathcal{L}(\text{data}|\mu, \hat{\alpha}(\mu))}{\mathcal{L}(\text{data}|\hat{\mu}, \hat{\alpha})} \,, \tag{8.7}$$

where $\hat{\alpha}(\mu)$ is the best fit for a given μ and $\hat{\alpha}$ is the best fit considering all possible values of μ. In this analysis, only systematic uncertainties that influence the normalisation of the distributions are taken into account. The implementation of shape-changing systematic uncertainties, such as the uncertainties on the jet energy scale and jet energy resolution, are beyond the scope of this thesis.

The application of the CLs criterion [70, 71],

$$CLs = \frac{p_{s+b}}{1 - p_b} = 5\% \,, \tag{8.8}$$

excludes all hypotheses with a signal rate larger than s at the 95% confidence level. This allows for the calculation of an upper limit on the cross section.

Table 8.1 contains the results for this analysis. The values represent the expected upper limit on the cross section of the signal and its uncertainties, when a theoretical signal cross section of 1 pb is assumed. If the expected upper limit is

Table 8.1: Upper limit on the cross section, assuming a signal cross section of 1 pb. All values in the table have units pb.

	-2σ	-1σ	Expected	$+1\sigma$	$+2\sigma$
LR	1.42	1.90	2.65	3.70	4.99
$H_{\mathrm{T}} + \not{E}_{\mathrm{T}}$	1.01	1.36	1.89	2.65	3.59
transformed LR	0.31	0.42	0.59	0.83	1.13

smaller than 1 pb, the signal process is excluded. The lower the upper limit, the more effective the discriminating variable.

The likelihood ratio in its original form has a worse expected upper limit than the simple variable $H_{\mathrm{T}} + \not{E}_{\mathrm{T}}$. When the sensitivity in the last bin of the likelihood ratio is spread over multiple bins, the expected upper limit drops by a factor 4.5. In this context, it is even possible to exclude the mass point at 95% confidence level. The expected limit with $H_{\mathrm{T}} + \not{E}_{\mathrm{T}}$ is about three times worse than that of the transformed likelihood ratio and does not allow this. The matrix element method is thus a valuable technique in the search for new physics.

The 'true' upper limits on the signal cross section are easily calculated. The numbers in Table 8.1 just need to be multiplied by the actual cross section of the signal sample.

9

Conclusions & Perspectives

In this thesis, the matrix element method was examined as an alternative technique to multivariate analyses for new-physics searches. Its performance was tested with respect to that of a simple kinematic variable, $H_{\mathrm{T}} + \not{E}_{\mathrm{T}}$, by calculating the upper limit on the cross section of the production of a stop quark pair decaying to a top quark and a neutralino. To simplify the interpretation of the results, the theoretical cross section of this process was assumed to be 1 pb. Whereas the simple likelihood ratio of the probabilities obtained by the matrix element method recorded a worse performance than the variable $H_{\mathrm{T}} + \not{E}_{\mathrm{T}}$, returning an expected upper limit of $2.65^{+1.05}_{-0.74}$ pb on the signal cross section compared to $1.89^{+0.76}_{-0.54}$ pb for $H_{\mathrm{T}} + \not{E}_{\mathrm{T}}$, a transformation of the likelihood ratio yielded an expected upper limit of $0.59^{+0.24}_{-0.17}$ pb. This is about a factor three better than the upper limit obtained by $H_{\mathrm{T}} + \not{E}_{\mathrm{T}}$ and proves that the matrix element technique is a valuable addition to the current analysis techniques searching for new physics and processes with a low signal-to-background ratio in general.

In the set-up of this analysis, the investigated mass point, having a stop quark mass of 350 GeV and a neutralino mass of 100 GeV, can be excluded at 95% confidence level, as was to be expected from the general CMS and ATLAS results displayed in Figures 2.5 and 2.6. This remark has to be treated with caution, however. As not all systematic uncertainties were included in this analysis, a comparison with other CMS and ATLAS results is not possible. Therefore, a comparison with a simple kinematic variable, treated on the same level as the matrix element method, was included in this analysis.

The results of this analysis can be improved on multiple levels. Firstly, a correction of the normalisation factors will allow a probabilistic interpretation of the quantities obtained by Equation (7.1). To this purpose, the transfer functions have to be normalised and the normalising cross section needs to be calculated at leading-order level. Even better results could be obtained if, instead of downgrading the precision of the cross section, the matrix element was calculated at

NLO level. Also more transfer functions can be added to include a more precise description of the detector effects. Of course, a balance between speed and accuracy has to be made. In any case, an upgrade to the new MadWeight version is recommended, as the time performance is tremendously improved. Efforts to make further improvements definitely have an impact on the precision of the analysis, as a quicker processing will reflect itself in the inclusion of more accurate transfer functions and higher-order matrix elements.

Secondly, the addition of shape-changing systematic uncertainties, such as the uncertainties on the jet energy scale, the jet energy resolutions, the b-tag scale factors and the pile-up reweighting, will give a more realistic value of the upper limit on the cross section and allow a comparison with other measurements.

Note that an increase in the collected integrated luminosity, which reduces the statistical uncertainty, is not always the best road to a better result. For this analysis, for example, the processing time is tremendously dependent on the number of events. Small improvements in accuracy, like the ones mentioned above, could yield a better result for a smaller subset of events in less time.

10

Summary

This analysis has successfully established that the matrix element method is a suitable technique for new physics searches. The investigated new physics was represented by a simplified supersymmetric model with direct stop quark production, where a stop quark of 350 GeV decayed into a top quark and a neutralino of 100 GeV.

The signal and its main backgrounds—$\mathrm{t\bar{t}}$ production, single top and W/Z+jets—were simulated to correctly estimate the contributions of each process. Only events with a semi-muonic decay were selected in this analysis. Additional selection criteria require, amongst others, exactly one isolated muon with a transverse momentum larger than 25 GeV, at least four jets with a $p_{\mathrm{T}} > 30\,\mathrm{GeV}$, of which two are identified as b jets, a missing transverse energy larger than 70 GeV and $H_{\mathrm{T}} > 250\,\mathrm{GeV}$.

The selected events from the simulated $\mathrm{t\bar{t}}$ sample were then used to estimate the mass of the W boson and the top quark. To this purpose, the observed jets were matched with the generated quarks. A χ^2 method that makes use of these masses then determined the optimal jet combination, without explicitly using the parton information. This ensured that the observed data events were treated on the same level as the simulated events. For the $\mathrm{t\bar{t}}$ events, the χ^2 method had an efficiency of 74% for choosing the correct jet-quark assignment.

The matrix element method reflects the probability that an event is produced and observed assuming a certain theoretical model. Detector effects are taken into account by transfer functions. For each event there are two model hypotheses. The first is that it is a signal event, i.e. a stop quark pair, the second that it is a background event, which will be represented by a top quark pair, as this is the most abundant background process. The probabilities are calculated for both cases and then combined into a discriminating variable, i.e. the transformed likelihood ratio $-\log\left[1 - \mathrm{P}(S)/(\mathrm{P}(S) + \mathrm{P}(B))\right]$.

The performance of the matrix element method is quantified by an upper limit on the production cross section of the signal. With the aid of a statistical method based on the profile likelihood ratio and the CLs criterion that is used for searches at the LHC, an expected upper limit of $0.59^{+0.24}_{-0.17}$ pb is obtained for the transformed likelihood ratio, where the theoretical signal cross section is assumed to be 1 pb. This means that the exclusion of the signal point under study is expected.

To be able to compare this result with other CMS studies, a full systematic investigation is necessary. This is beyond the scope of this thesis and, instead, a comparison with a simple kinematic variable, $H_{\mathrm{T}} + \not{E}_{\mathrm{T}}$, is made. Using the same statistical method, an upper limit of $1.89^{+0.76}_{-0.54}$ pb is obtained, which is about three times higher. This proves that the matrix element method is more sensitive to the signal than this simple kinematic variable and that this technique is viable to look for new physics.

Samenvatting

Deze analyse toont aan dat de matrix element methode geschikt is om naar nieuwe fysica te zoeken. Om dit na te gaan werd een vereenvoudigd supersymmetrisch model met de rechtstreekse productie van een stop quark paar onderzocht. Enkel het geval waar een stop quark met een massa van 350 GeV in een top quark en een neutralino van 100 GeV vervalt werd beschouwd.

Het signaal en de voornaamste achtergrondprocessen—top quark paarproductie, enkelvoudige top quark productie en W- of Z+jets—werden gesimuleerd om de bijdrage van elk proces correct te kunnen inschatten. Enkel gebeurtenissen die voldeden aan de bepaalde voorwaarden werden beschouwd. De geselecteerde gebeurtenissen hadden exact één geïsoleerd muon met een transversaal impuls p_{T} groter dan 25 GeV en ten minste vier jets met een $p_{\mathrm{T}} > 30\,\mathrm{GeV}$, waarvan er twee als b-jet geïdentificeerd werden. Verder moest de ontbrekende transversale energie $\not{E}_{\mathrm{T}}$ groter zijn dan 70 GeV en de scalaire som van de transversale impulsen van de vier hardste jets $H_{\mathrm{T}} > 250\,\mathrm{GeV}$.

De geselecteerde $\mathrm{t\bar{t}}$-gebeurtenissen werden gebruikt om de massa van het W-boson en de top quark te schatten. Hiervoor werden de geselecteerde jets gepaard met de gegenereerde quarks. Een χ^2-methode die deze massa's aanwendt, bepaalde de optimale jet-quark associatie, evenwel zonder expliciet de informatie van de gegenereerde quarks te gebruiken. Dit garandeerde dat de geobserveerde gebeurtenissen op gelijke voet behandeld werden als de gesimuleerde gebeurtenissen. Voor de $\mathrm{t\bar{t}}$-gebeurtenissen koos de χ^2-methode de juiste jet-quark combinatie in 74% van de gevallen.

De matrix element methode geeft de waarschijnlijkheid weer dat een gebeurtenis geproduceerd en geobserveerd wordt wanneer een bepaald theoretisch model wordt ondersteld. Detectoreffecten worden in rekening gebracht door het gebruik van transferfuncties. Er zijn twee hypotheses voor elke gebeurtenis, ofwel is de gebeurtenis afkomstig van signaal, nl. een stop quark paar, ofwel van een achtergrondproces. Het achtergrondproces wordt voorgesteld als een top quark paar, aangezien dit de meest voorkomende achtergrondgebeurtenis is. Met behulp van de matrix element methode werden de waarschijnlijkheden berekend voor beide hypotheses en dan gecombineerd in een variabele die gevoelig is voor het signaal, nl. de getransformeerde likelihood ratio $-\log\left[1-\mathrm{P}(S)\,/(\mathrm{P}(S)+\mathrm{P}(B))\right]$.

De performantie van de matrix element methode werd gekwantificeerd door een bovenlimiet op de werkzame doorsnede van het signaal. Met behulp van statistische methoden gebaseerd op de 'profile likelihood ratio' en het 'CLs criterium' dat gebruikt wordt voor het zoeken naar nieuwe fysica aan de Large Hadron Collider, werd een verwachte bovenlimiet van $0.59^{+0.24}_{-0.17}$ pb verkregen voor de getransformeerde likelihood ratio wanneer verondersteld werd dat de theoretische werkzame doorsnede van het signaal 1 pb is.

Om dit resultaat te kunnen vergelijken met andere zoektochten naar stop quark productie in de CMS collaboratie is een grondige studie van alle systematische effecten nodig. Dit behoort niet tot de doelstelling van deze thesis. In plaats daarvan werd een vergelijking met een simpele kinematische variabele, $H_{\mathrm{T}}+\not{E}_{\mathrm{T}}$, gemaakt. Met dezelfde statistische methode werd een verwachte bovenlimiet van $1.89^{+0.76}_{-0.54}$ pb verkregen. Dit ligt ongeveer drie keer hoger dan de bovenlimiet bekomen met de getransformeerde likelihood ratio en bewijst dat de matrix element methode gevoeliger is voor het signaal dan deze kinematische variabele. Deze methode is dus nuttig in de zoektocht naar nieuwe fysica.

Acknowledgements

First of all, I want to thank my promotor Jorgen D'Hondt and the Inter-university Institute for High-Energies (IIHE) for giving me the opportunity to make an interesting thesis. The world of particle physics is a fascinating one, with many roads to travel. The endless possibilities make it easy to lose the overview, but your guidance kept me on track.

I am greatly indebted to Dr. Petra Van Mulders, who was always there to help me and bravely defied the—in my eyes—endless stream of questions.

Many thanks to Annik Olbrechts who introduced me to `MadWeight/MadGraph`, Stijn Blyweert and Michael Maes for helping me to solve some of my programming issues and Olivier Devroede for sorting out my priority on the cluster.

Additional thanks to all PhD students and post-docs in our cosy greenhouse for their kind words of consolation in times of need, their offers of help and, not in the least, the amazing lunchtime conversations.

During my studies I met some amazing people. Thank you, Isabelle, Isis, Kevin, Ivo, Mathias, Bert, ... for making life just a little more pleasurable.

Though mentioned before, special thanks are needed for Isis Van Parijs, who, even in her gloomiest moments, gave me the courage to go on, these last hectic weeks. Many a lonely hour was spent at the office with frantic working and a sprinkle of synchronised sighing concertos.

Further, I want to thank Tom Bauwens for reminding me that there is also a life next to the thesis (and hopefully also afterwards) and my parents for offering to proofread my text and the many gestures of mental support (thunderstorms!)

References

[1] S. P. Martin, *A Supersymmetry Primer*, `arXiv:hep-ph/9709356`.

[2] *The University of Tennessee, Knoxville, Department of Physics and Astronomy*, `http://electron6.phys.utk.edu/phys250/modules/module%206/particle_classification.htm`.

[3] *Particle Data Group*, `http://pdg.lbl.gov/`.

[4] E. Fiorini, *Neutrino: Dirac or Majorana?*, in *Ettore Majorana's legacy and the Physics of the XXI century.* Catania, Italy, October, 2006. PoS(EMC2006)007.

[5] D. J. Griffiths, *Introduction to Elementary Particles.* Wiley-VCH, 2 ed., 2011.

[6] F. Englert and R. Brout, Phys. Rev. Lett. **13** (1964) 321–322.

[7] P. Higgs, Phys. Rev. Lett. **13** (1964) 508–509.

[8] G. Guralnik, C. Hagen, and T. Kibble, Phys. Rev. Lett. **13** (1964) 585–587.

[9] N. Polonsky, *Supersymmetry: Structure and Phenomena*, `arXiv:hep-ph/0108236`.

[10] D. Bailin, G. V. Kraniotis, and A. Love, Phys.Lett. **B414** (1997) 269–276.

[11] The CMS Collaboration, *Interpretation of searches for supersymmetry with simplified models*, Tech. Rep. arXiv:1301.2175. CMS-SUS-11-016. CERN-PH-EP-2012-351, CERN, Geneva, Jan, 2013. Comments: Submitted to Phys. Rev. D.

[12] The CMS Collaboration, *Search for top-squark pair production in the single lepton final state in pp collisions at 8 TeV*, Tech. Rep. CMS-PAS-SUS-13-011, CERN, Geneva, 2013.

[13] The ATLAS Collaboration, *ATLAS Physics Summary Plots*, `https://twiki.cern.ch/twiki/bin/view/AtlasPublic/CombinedSummaryPlots#SusyDirectStopSummary`.

[14] CERN, *Cryogenics: Low temperatures, high performance*, `http://home.web.cern.ch/about/engineering/cryogenics-low-temperatures-high-performance`.

[15] CERN, *LHC, the guide*, `http://cds.cern.ch/record/1165534/files/CERN-Brochure-2009-003-Eng.pdf`, 2009.

[16] M. Della Negra, L. Foà, A. Hervé, and A. Ball, *CMS physics Technical Design Report*. Technical Design Report CMS. CERN, Geneva, 2006.

[17] The ALICE Collaboration, JINST **3 S08002** (2008).

[18] The ATLAS Collaboration, JINST **3 S08003** (2008).

[19] The CMS Collaboration, JINST **3 S08004** (2008).

[20] The LHCb Collaboration, JINST **3 S08005** (2008).

[21] The LHCf Collaboration, JINST **3 S08006** (2008).

[22] The TOTEM Collaboration, JINST **3 S08007** (2008).

[23] The CMS Collaboration, C. Mariotti, *Recent results on Higgs studies at CMS*, `http://indico.cern.ch/getFile.py/access?contribId=1&resId=0&materialId=slides&confId=245795`, April, 2013.

[24] The CMS Collaboration, *Detector overview: Superconducting Magnet*, `http://cms.web.cern.ch/news/superconducting-magnet`.

[25] *The University of Tennessee, Knoxville, High Energy Physics Group*, `http://hep.phys.utk.edu/~spanier/CMS/CMS_3D_Detector_50.gif`.

[26] The CMS Collaboration, *Detector overview: Tracker detector*, `http://cms.web.cern.ch/news/tracker-detector`.

[27] M. Chen, *Scintillation and Light Sensitive Detectors*, `http://neutron.physics.ucsb.edu/docs/scintillation_presentation_info.pdf`.

[28] The CMS Collaboration, *Detector overview: Hadron Calorimeter*, `http://cms.web.cern.ch/news/hadron-calorimeter`.

[29] M. Della Negra and E. Radermacher, *CMS: The Hadron Calorimeter*. Technical Design Report CMS. CERN, Geneva, 1997.

[30] The CMS Collaboration, *Detector overview: Crystal Calorimeter*, `http://cms.web.cern.ch/news/crystal-calorimeter`.

[31] The CMS Collaboration, *Detector overview: Electromagnetic Calorimeter*, `http://cms.web.cern.ch/news/electromagnetic-calorimeter`.

[32] M. Della Negra and E. Radermacher, *CMS: The Muon Project*, pp. 249–309. Technical Design Report CMS. CERN, Geneva, 1997.

[33] The CMS Collaboration, *Detector overview: Resistive Plate Chambers*, `http://cms.web.cern.ch/news/resistive-plate-chambers`.

[34] P. Zotto, *CMS Muon System Overview, 5th International Workshop on B-Physics at Hadron Machines*, `http://www.pd.infn.it/~zotto/beauty97/rpc.html`, 1997.

[35] The CMS Collaboration, *Detector overview: Muon Drift Tubes*, `http://cms.web.cern.ch/news/muon-drift-tubes`.

[36] The CMS Collaboration, *Detector overview: Cathode Strip Chambers*, `http://cms.web.cern.ch/news/cathode-strip-chambers`.

[37] M. Della Negra, A. Hervé, S. Cittolin, W. H. Smith, and J. Varela, *The TriDAS Project Technical Design Report, Volume 1: The Trigger Systems,*.

[38] The CMS Collaboration, *Particle-Flow Event Reconstruction in CMS and Performance for Jets, Taus, and MET*, Tech. Rep. CMS-PAS-PFT-09-001, CERN, Geneva, 2009.

[39] The CMS Collaboration, D. Barney, *Animated CMS slice for Powerpoint*, `https://cms-docdb.cern.ch/cgi-bin/PublicDocDB/ShowDocument?docid=5581`.

[40] W. Adam, B. Mangano, T. Speer, and T. Todorov, *Track reconstruction in the CMS Tracker*, CMS NOTE-2006/041.

[41] S. Cucciarelli, M. Konecki, D. Kotliński, and T. Todorov, *Track reconstruction, primary vertex finding and seed generation with the Pixel Detector*, CMS NOTE-2006/026.

[42] R. Frühwirth, Nuclear Instruments and Methods in Physics Research Section A: Accelerators, Spectrometers, Detectors and Associated Equipment **262** (1987), no. 23, 444 – 450. `http://www.sciencedirect.com/science/article/pii/0168900287908874`.

[43] G. Abbiendi, A. Adam, J. Alcaraz, *et al.*, *Muon Reconstruction in the CMS Detector*, CMS AN-2008/097.

[44] The CMS Collaboration, *Commissioning of the Particle-flow Event Reconstruction with the first LHC collisions recorded in the CMS detector*, Tech. Rep. CMS-PAS-PFT-10-001, CERN, Geneva, 2010.

[45] W. Adam, R. Frühwirth, A. Strandlie, and T. Todor, *Reconstruction of Electrons with the Gaussian-Sum Filter in the CMS Tracker at the LHC*, Tech. Rep. CMS-NOTE-2005-001, CERN, Geneva, 2005.

[46] S. Baffioni, C. Charlot, F. Ferri, *et al.*, *Electron Reconstruction in CMS*, CMS NOTE 2006/40.

[47] M. Pioppi, *Electron Pre-identification in the Particle Flow framework*, CMS AN-2008/032.

[48] M. Cacciari, G. P. Salam, and G. Soyez, JHEP **2008** (2008), no. 04, 063.

[49] The CMS Collaboration, J. Instrum. **8 P04013** (Nov, 2012) P04013. 67 p. arXiv:hep-ex/1211.4462. CMS-BTV-12-001. CERN-PH-EP-2012-262.

[50] J. Alwall, M. Herquet, F. Maltoni, *et al.*, JHEP **2011** (2011), no. 06, 128.

[51] P. Nason, JHEP **2004** (2004), no. 11, 040.

[52] S. Frixione, P. Nason, and C. Oleari, JHEP **2007** (2007), no. 11, 070.

[53] S. Alioli, P. Nason, C. Oleari, and E. Re, JHEP **2009** (2009), no. 09, 111.

[54] T. Sjöstrand, P. Edén, C. Friberg, *et al.*, Computer Physics Communications **135** (2001), no. 2, 238 – 259.

[55] B. Andersson, *The Lund Model*, vol. 7 of *Cambridge Monographs on Particle Physics, Nuclear Physics and Cosmology.* Cambridge University Press, 2005.

[56] S. Agostinelli, J. Allison, K. Amako, *et al.*, Nuclear Instruments and Methods in Physics Research Section A: Accelerators, Spectrometers, Detectors and Associated Equipment **506** (2003), no. 3, 250 – 303.

[57] J. Allison, K. Amako, J. Apostolakis, *et al.*, Nuclear Science, IEEE Transactions on **53** (2006), no. 1, 270–278.

[58] N. Kidonakis, *NNLL threshold resummation for top-pair and single-top production*, `1210.7813`.

[59] R. Gavin, Y. Li, F. Petriello, and S. Quackenbush, *W physics at the LHC with FEWZ 2.1*, ANL-HEP-PR-11-83, NUHEP-TH/12-01, PSI-PR-12-01, arXiv:hep-ph/1201.5896.

[60] R. Gavin, Y. Li, F. Petriello, and S. Quackenbush, Computer Physics Communications **182** (2011), no. 11, 2388 – 2403.

[61] The ATLAS Collaboration, M. Bianco, E. Gorini, M. Primavera, and A. Ventura, *Scale Factors for Muon Trigger Efficiency on 2012 ATLAS data*, `http://annualreport.dmf.unisalento.it/2012/experiment/ScaleFactors_ventura.pdf`.

[62] J. C. Estrada Vigil, *Maximal Use of the Kinematic Information for the Extraction of the Mass of the Top Quark in Single-lepton* $t\bar{t}$ *Events at DØ*. PhD thesis, University of Rochester, Rochester, New York, 2001. `http://www-d0.fnal.gov/results/publications_talks/thesis/estrada/thesis.ps`.

[63] The DØ Collaboration, Nature **429** (June, 2004) 638–642.

[64] O. Mattelaer, *A new approach to matrix element reweighting*. PhD thesis, Université Catholique de Louvain, Louvain-la-Neuve, 2011. `http://cp3.irmp.ucl.ac.be/upload/theses/phd/mattelaer.pdf`.

[65] P. Artoisenet and O. Mattelaer, *MadWeight: automatic event reweighting with matrix elements*, in *Prospects for Charged Higgs Discovery at Colliders*. Uppsala, Sweden, September, 2008. PoS(CHARGED2008)025.

[66] P. Artoisenet, V. Lemaître, F. Maltoni, and O. Mattelaer, *MadWeight Wiki*, `https://cp3.irmp.ucl.ac.be/projects/madgraph/wiki/MadWeight`.

[67] J. Thaler, *LHCO format*, `http://madgraph.phys.ucl.ac.be/Manual/lhco.html`.

[68] *Procedure for the LHC Higgs boson search combination in summer 2011*, Tech. Rep. ATL-PHYS-PUB-2011-011, CERN, Geneva, Aug, 2011.

[69] G. Cowan, K. Cranmer, E. Gross, and O. Vitells, The European Physical Journal C **71** (2011), no. 2, 1–19. arXiv:1007.1727.

[70] A. L. Read, J. Phys. **G28** (2002) 2693.

[71] T. Junk, Nucl. Instrum. Meth. **A434** (1999) 435.

[72] G. P. Salam, *Towards Jetography*, `arXiv:hep-ph/09061833`.

List of Abbreviations

ALICE	A Large Ion Collider Experiment
APD	Avalanche photodiode
ATLAS	A Toroidal LHC ApparatuS
BR	Branching ratio
BSM	Beyond the standard model
CERN	European Organization for Nuclear Research (Conseil Européen pour la Recherche Nucléaire)
CMS	Compact Muon Solenoid
cMSSM	Constrained MSSM or minimal supergravity (mSUGRA)
CP	Charge conjugation and Parity
CSC	Cathode strip chamber
CSV	Combined Secondary Vertex algorithm for b-tagging
CSVM	Combined Secondary Vertex algorithm with medium working point. This allows a mistagging rate of about 1% at p_{T} values of 80 GeV.
DAQ	Data aquisition system
DT	Drift tube
ECAL	Electromagnetic calorimeter
FEWZ	Fully Exclusive W and Z Production, for the calculation of cross sections
GEANT4	GEometry ANd Tracking, version 4
GUT	Grand unified theory
HCAL	Hadron calorimeter

HLT	High-level trigger
HPD	Hybrid photodiodes
IRC	Infrared and collinear safety of a jet algorithm
L1	Level-1 trigger
LEIR	Low Energy Ion Ring
LHC	Large Hadron Collider
LHCb	Large Hadron Collider beauty
LHCf	Large Hadron Collider forward
LO	Leading order
LR	Likelihood ratio
LSP	Lightest supersymmetric particle
MC	Monte Carlo simulation
MEM	Matrix element method
MSSM	Minimal Supersymmetric Standard Model
mSUGRA	Minimal supergravity or constrained MSSM (cMSSM)
MVA	Multivariate analysis technique
NLO	Next-to-leading order
PF	Particle Flow algorithm
PLR	Profile likelihood ratio
pMSSM	Phenomenological MSSM
POWHEG	POsitive Weight Hardest Emission Generator
PS	Proton Synchrotron
PU	Pile-up
PV	Primary vertex
relIso	Relative isolation (of a lepton)
RMS	Root-mean-square
RPC	Resistive plate chamber

SM	Standard model
SPS	Super Proton Synchrotron
ST	Single top
SUSY	Supersymmetry
SV	Secondary vertex
TOTEM	TOTal Elastic and diffractive cross section Measurement
VPT	Vacuum phototriode

Appendix A

Jet Reconstruction Algorithms

Quarks have a natural tendency to form colourless combinations. When they are produced in particle collisions, they will first fragment and consequently hadronise. The produced showers of particles will be organised into well-defined jets that represent the original quark. The properties of this jet give a good indication of what the properties of the quark would have been.

There are several methods to organise particles into jets, which can be classified into iterative cone algorithms and sequential recombination algorithms. The first uses a top-down approach, while the latter is a bottom-up algorithm.

A.1 Iterative Cone Algorithms

Cone algorithms start from a seed particle, usually that with the highest transverse momentum. Then an imaginary cone with a radius R around the seed is taken and all particles within this cone are included in the jet. This procedure is iteratively repeated. Several possibilities exist to avoid overlaps between different jets. The progressive removal approach (IC-PR) removes all particles contained in the jet from the event before it will search a new seed. The split-merge approach (IC-SM) will first construct all cones, called protojets. Depending on the extent of shared transverse momentum, i.e. particles, between the protojets, they will be merged into one jet or split into separate jets. The problem of the latter technique is that it suffers from infrared unsafety. This means that soft particle radiation can alter the set of jets and is illustrated in Figure A.1 [72]. Whereas the soft radiation in Figure A.1(b) has no effect, in Figure A.1(c) only one jet is reconstructed.

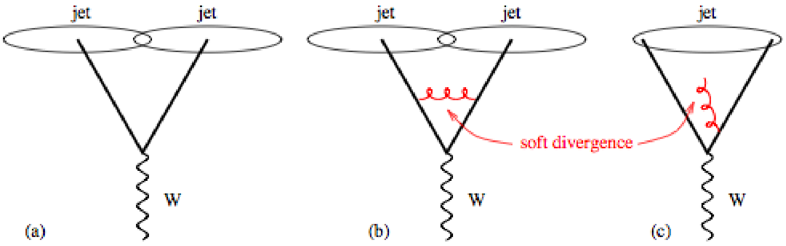

Figure A.1: Illustration of infrared unsafety for an IC-SM type algorithm, using an event with a W boson and two hard partons (a) without soft radiation; (b) with a soft divergence that does not influence the final jet states; (c) with a soft divergence that influences the final jet states.

The IC-PR algorithm, on the other hand, suffers from collinear unsafety. As it progressively removes the jets formed by the hardest seed, a collinear split of a particle can alter the jet formation. This is illustrated in Figure A.2 [72].

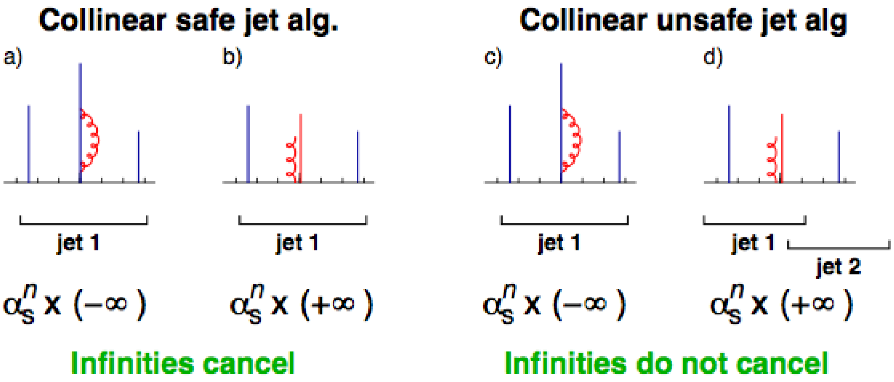

Figure A.2: Illustration of collinear safety and unsafety for an IC-PR type algorithm. The height of the partons is proportional to their transverse momentum

A.2 Sequential Recombination Algorithms

Another approach to jet making is sequential recombination. Here, the distances d_{ij} between all particles or pseudojets i and j and the distances d_{iB} between entity i and the beam are determined and the smallest distance is identified. If it is of type d_{ij}, entities i and j will be recombined into a pseudojet and the distances will be recalculated. If it is of type d_{iB}, i is called a jet and removed from the list.

The distances are defined as

$$\begin{aligned} d_{iB} &= k_{\mathrm{T},i}^{2p}\,, \\ d_{ij} &= \min\left(k_{\mathrm{T},i}^{2p}, k_{\mathrm{T},j}^{2p}\right)\frac{\Delta_{ij}^2}{R^2}\,, \qquad \Delta_{ij}^2 = (y_i - y_j)^2 + (\phi_i - \phi_j)^2\,, \end{aligned} \tag{A.1}$$

where $k_{\mathrm{T},i}$ is the transverse momentum, ϕ_i is the azimuthal angle and $y_i \equiv \frac{1}{2}\ln\frac{E+p_z}{E-p_z}$ is the rapidity of particle i. R is a radius parameter of the same sort as the one used for iterative cone algorithms, while p controls the relative power of the energy compared to the geometrical scale Δ_{ij}. When $p = 1$ the algorithm is called the (inclusive) k_{T} algorithm, when $p = 0$ it is called the Cambridge/Aachen algorithm and when $p = -1$ the anti-k_{T} algorithm.

Appendix B

b-tag Scale Factors

Due to the properties of B hadrons, b jets can be differentiated from other jets. As algorithms are never perfect, there is always a chance that non-b jets are accidentally identified or ‘tagged’ as b jets. This mistag rate is different for jets originating from c quarks, which can produce hadrons with a medium lifetime, and light jets, which originate from u, d or s quarks and gluons. The efficiency to tag jets of flavour i is defined as the ratio of the number of tagged jets to the total number of jets of that flavour, i.e.

$$\epsilon_i = \frac{\text{Number of tagged jets of flavour } i}{\text{Total number of jets of flavour } i} \,. \tag{B.1}$$

As the tagging efficiency is different in data and simulation, scale factors SF_i were measured by the CMS collaboration. These scale factors depend on the jet flavour, p_{T} and η. Also the efficiency in simulation is obtained as a function of these quantities. This is visualised in Figure B.1.

The probability to tag a number of jets in events in simulation is defined as

$$\mathrm{P}(MC) = \prod_{\substack{i \\ \text{tagged}}} \epsilon_i \prod_{\substack{j \\ \text{not tagged}}} (1 - \epsilon_j) \,, \tag{B.2}$$

while in data this probability becomes

$$\mathrm{P}(\text{data}) = \prod_{\substack{i \\ \text{tagged}}} \mathrm{SF}_i \epsilon_i \prod_{\substack{j \\ \text{not tagged}}} (1 - \mathrm{SF}_j \epsilon_j) \,, \tag{B.3}$$

where i and j are elements of the collections of tagged and non-tagged jets respectively.

The b-tag weight assigned to a simulated event is then

$$w = \frac{\mathrm{P}(\text{data})}{\mathrm{P}(MC)} \,. \tag{B.4}$$

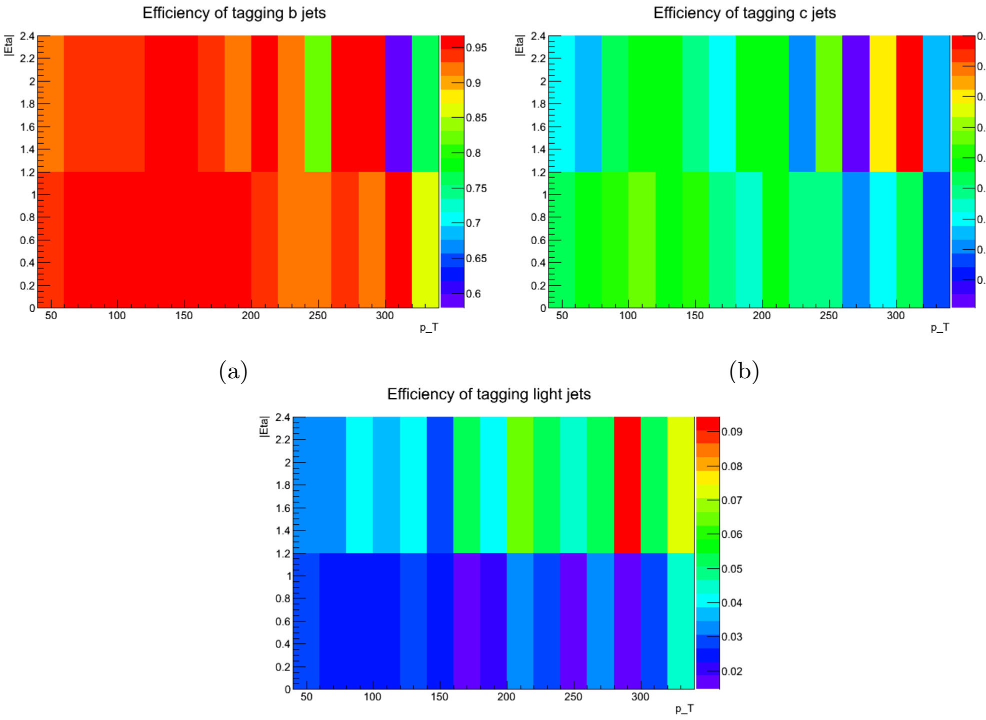

(a) (b)

(c)

Figure B.1: Efficiency of the CSV algorithm for (a) b jets; (b) c jets; (c) light jets. The last p_{T} bins contain the overflow.

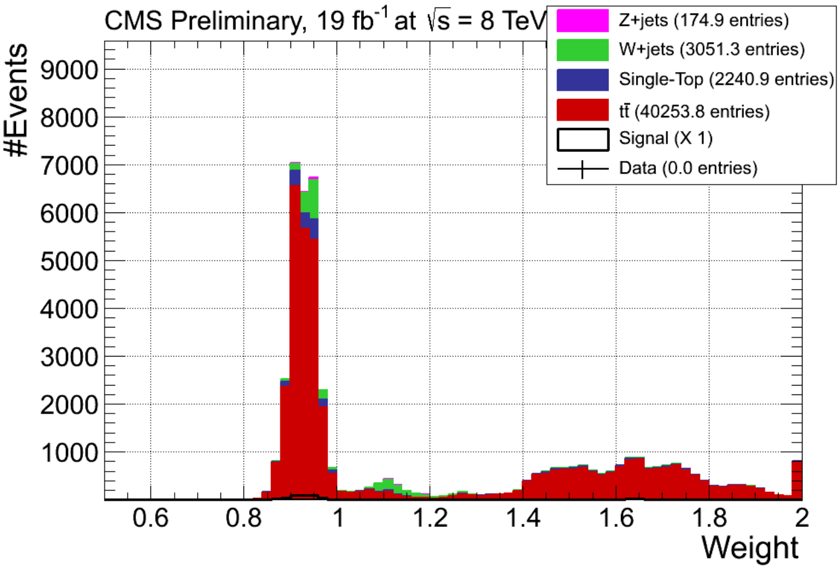

Figure B.2: Distribution of the b-tag weights assigned to the events. The last bin contains the overflow.

Appendix C

MadWeight Cards

C.1 Process Cards

The process card for $t\bar{t}$ production can be found below.

```
#************************************************************
#*                        MadGraph 5                        *
#*                                                          *
#*                *                       *                 *
#*                  *        * *        *                   *
#*                    * * * * 5 * * * *                     *
#*                  *        * *        *                   *
#*                *                       *                 *
#*                                                          *
#*                                                          *
#*         VERSION 2.0.0.beta1           2012-11-08         *
#*                                                          *
#*    The MadGraph Development Team - Please visit us at    *
#*    https://server06.fynu.ucl.ac.be/projects/madgraph     *
#*                                                          *
#************************************************************
#*                                                          *
#*               Command File for MadGraph 5                *
#*                                                          *
#*     run as ./bin/mg5  filename                           *
#*                                                          *
#************************************************************

set group_subprocesses Auto
set ignore_six_quark_processes False
set loop_optimized_output True
set gauge unitary
set complex_mass_scheme False
import model sm
define p = g u c d s u~ c~ d~ s~
define j = g u c d s u~ c~ d~ s~
define l+ = e+ mu+
define l- = e- mu-
define vl = ve vm vt
define vl~ = ve~ vm~ vt~
define p u u~ d d~ s s~ c c~ b b~ g
generate p p > t t~ , t > b mu+ vm , t~ > b~ j j @1
```

To generate a stop quark pair, the MSSM has to be included. In order to only generate processes where the stop quark decays into a top quark and a neutralino, some processes are excluded by hand.

```
#************************************************************
#*                        MadGraph 5                        *
#*                                                          *
#*                *                       *                 *
#*                  *        * *        *                   *
#*                    * * * * 5 * * * *                     *
#*                  *        * *        *                   *
#*                *                       *                 *
#*                                                          *
#*                                                          *
#*         VERSION 2.0.0.beta1           2012-11-08         *
#*                                                          *
#*    The MadGraph Development Team - Please visit us at    *
#*    https://server06.fynu.ucl.ac.be/projects/madgraph     *
#*                                                          *
#************************************************************
#*                                                          *
#*               Command File for MadGraph 5                *
#*                                                          *
#*     run as ./bin/mg5  filename                           *
#*                                                          *
#************************************************************

set group_subprocesses Auto
set ignore_six_quark_processes False
set loop_optimized_output True
set gauge unitary
set complex_mass_scheme False
import model sm
define p = g u c d s u~ c~ d~ s~
define j = g u c d s u~ c~ d~ s~
define l+ = e+ mu+
define l- = e- mu-
define vl = ve vm vt
define vl~ = ve~ vm~ vt~
import model mssm
define p u u~ d d~ s s~ c c~ b b~ g
define s1 ul ul~ ur ur~ dl dl~ dr dr~ sl sl~ sr sr~ cl cl~ cr cr~
define s3 b1 b1~ b2 b2~ t2 t2~
define sch x1+ x2+ x1- x2-
generate p p > t1 t1~ / sch s1 s3 , t1 > b mu+ vm n1 / sch s1 s3  , t1~ > b~ j j n1 / sch s1 s3 @1 # 12 diagrams
```

C.2 Transfer Function

```
<file>## ##############################################################
##                                                                ##
##                  Generate the transfer functions               ##
##                  -------------------------------               ##
##                                                                ##
##    Authors: Mattelaer Olivier (UCL-CP3/ROMA3-INFN)             ##
##             Artoisenet Pierre (OHIO)                           ##
##    Version:     2.0.0                                          ##
##    Last change: 22/09/09                                       ##
##                                                                ##
####################################################################

##**********************************************************##
##                          TF b JET                        ##
##**********************************************************##
<block name='jet'>   #name can be anything
<info> doubel gaussian with parameter depending of the energy </info>
<particles> u,d,s,c,g,b </particles>
# this defined when this tf will be used.the letter correspond to the label
#          in particles.dat
<width_type> large </width_type>
# width_type should be thin or large (thin is for energy accurate up to 5-10%)
<variable name='E'>
<tf>
        IF ((btag(1) .GT. 0.0) .OR. (btag(4) .GT. 0.0))THEN
          prov1=(#1+#2*dsqrt(p(0))+#3*p(0))
          prov2=(#4+#5*dsqrt(p(0))+#6*p(0))
          prov3=(#7+#8*dsqrt(p(0))+#9*p(0))
          prov4=(#10+#11*dsqrt(p(0))+#12*p(0))
          prov5=(#13+#14*dsqrt(p(0))+#15*p(0))
          prov6=(#16+#17*dsqrt(p(0))+#18*p(0))
  ELSE
          prov1=(#19+#20*dsqrt(p(0))+#21*p(0))
          prov2=(#22+#23*dsqrt(p(0))+#24*p(0))
          prov3=(#25+#26*dsqrt(p(0))+#27*p(0))
          prov4=(#28+#29*dsqrt(p(0))+#30*p(0))
          prov5=(#31+#32*dsqrt(p(0))+#33*p(0))
          prov6=(#34+#35*dsqrt(p(0))+#36*p(0))
  ENDIF
  tf= prov3*(exp(-(p(0)-pexp(0)-prov1)**2/2d0/prov2**2))    !first gaussian
  tf=tf+prov6*exp(-(p(0)-pexp(0)-prov4)**2/2d0/prov5**2)    !second gaussian
</tf>
<width>
        IF ((btag(1) .GT. 0.0) .OR. (btag(4) .GT. 0.0))THEN
          prov2=(#4+#5*dsqrt(pexp(0))+#6*pexp(0))
          prov5=(#13+#14*dsqrt(pexp(0))+#15*pexp(0))
  ELSE
          prov2=(#22+#23*dsqrt(pexp(0))+#24*pexp(0))
          prov5=(#31+#32*dsqrt(pexp(0))+#33*pexp(0))
  ENDIF
  width=max(prov2,prov5)
</width>
</variable>
</block>
</file>
```

C.3 MadWeight Card

```
##############################################################################
##                                                                          ##
##                               MadWeight                                  ##
##                             =============                                ##
##                                                                          ##
##                              Run control                                 ##
##                              -----------                                 ##
##                                                                          ##
##                                                                          ##
##    Author: Mattelaer Olivier (UCL-CP3)                                   ##
##            Artoisenet Pierre (UCL-CP3)                                   ##
##                                                                          ##
##    Version:     1.1.5                                                    ##
##    Last change: 01/06/10                                                 ##
##                                                                          ##
##############################################################################
##                                                                          ##
##  This Card defines all specific parameters of Madweight                  ##
##                                                                          ##
##############################################################################
#*************************************************************************
##                      select run options                                  ##
#*************************************************************************
Block MW_Run
#   TAG                    VALUE                     UTILITY
     name                   TT_TTbar    # name for the run
     cluster                5       # 0:single machine, 1: condor, 2: SGE
                                    # 3: Bash cluster, 4: multiprocessor, 5: qsub
                                    # For more info, see the wiki
     queue        '-q localgrid@cream02 -l walltime=01:00:00' # queue condition (usage depend of the cluster)
     nb_exp_events          31606      # number of experimental events to consider
     write_log              F       # avoid writting of a lot of log files
     ME_int_points          10000   # number of points in MadEvent integration
     MW_int_points          30000   # number of points in MadWeight integration
     use_cut                F       # use the cut defined in run_card.dat
     bw_cut                 F       # use the BW cut
     nwa                    F       # T= use narrow width approximation
     isr                    2       # isr=0 : ignore ISR effect (except if all FS particles are visible)
                                    # isr=1 : correct kinematic based on reconstructed Pt(isr)
                                    # isr=2 : correct kinematic based on reconstructed Pt(isr)
                                    #         + boost the weight to the CMS frame

#*************************************************************************
##                  define the different param_card's                       ##
#*************************************************************************
Block MW_parameter
#   TAG       VALUE                     UTILITY
    mode         0            #    type of input
                            #    0 : inputs are read from the cards: param_card_1.dat, param_card_2.dat,...
```

```
                        #    1 : redefines some values from param_card.dat according to the form below
                              #    2 : same but the value for different parameters are modified simultaneously
#
#                                # first parameter #
#     11        mass            # Block of the parameter to change
#     12        6               # id of the parameter to change
#     13        180             # here you can enter the different values:
#     13        190             #  add a new line with tag 13 to introduce a new value
#
#                               #  second parameter #
#                               !DELETE ALL THE FOLLOWING TAG IF YOU WANT TO RUN WITH ONLY ONE PARAM!
#     21        MGCKM            # Block of the parameter to change
#     22        1                # id of the paramter to change
#     22        2                # id2 of the paramter to change
#     23        1.5E-02          # here you can enter the different values:
#     23        1.8E-02          # add a new line with tag 23 to introduce a new value
#
#  use same syntax for parameters 3,4,...
#*********************************************************************
##                          Permutations                           ##
#*********************************************************************
Block MW_perm
#   TAG            VALUE                    UTILITY
     permutation   F         # make permutation
     bjet_is_jet   T         # consider permutation between b-jets and light jets
```

Een nieuwe aanpak van de zoektocht naar stop quarks aan de Large Hadron Collider met behulp van de matrixelementmethode

Sinds de ontdekking van het Higgs deeltje in 2012 is het standaard model der deeltjes weer op het voorplan verschenen. Ondanks zijn opmerkelijke overeenkomst met experimentele resultaten kan dit model niet alles verklaren. Een mogelijke oplossing voor tal van onopgeloste vragen is de introductie van een nieuwe symmetrie, "supersymmetrie", die deeltjes en krachten op gelijke voet behandelt. Deze theorie voorspelt een heleboel nieuwe deeltjes, maar die zijn tot op heden nog niet geobserveerd. Indien ze bestaan, worden deze deeltjes slechts zeer zelden geproduceerd, zo zelden dat ze lijken te verdrinken in een achtergrond van standaard model processen. Er is dus nood aan technieken die dit kleine signaal uit de achtergrond kunnen filteren. Een nieuwe methode die hiertoe kan bijdragen is de matrixelementmethode.

Wanneer twee deeltjes botsen in de Large Hadron Collider (LHC) worden er nieuwe deeltjes gecreëerd, die op hun beurt weer vervallen naar andere deeltjes. Alle informatie over zo'n proces, zoals de energie en massa van de deeltjes, zit vervat in een zogenoemd matrixelement. Aangezien een detector niet perfect is, zijn de gemeten energieën vaak verschillend van de echte energieën van de deeltjes. Dit wordt in rekening gebracht door transferfuncties, die het verband geven tussen de geobserveerde en de echte energieën van de deeltjes. Als er rekening gehouden wordt met hoe vaak een bepaald proces geproduceerd wordt, ook wel werkzame doorsnede genoemd, geeft de matrixelementmethode de waarschijnlijkheid weer dat het geobserveerde proces signaal of achtergrond is.

Op deze manier kan een bovengrens voor de werkzame doorsnede van de signaalprocessen bepaald worden. Hoe strenger deze bovenlimiet, des te gevoeliger is de methode voor het signaal. Met de matrixelementmethode werd een bovengrens bekomen die ongeveer driemaal kleiner is dan deze verkregen met andere technieken, die slechts een gedeelte van de informatie van het proces gebruiken. Dit betekent dat de matrixelementmethode uitermate nuttig is in de zoektocht naar nieuwe fysica.